

Dynamics and multi-stability of a rotor-actuated Twistcar robot with passive steering joint

Anna Zigelman* · Zitao Yu · Rom Levy · Yizhar Or

the date of receipt and acceptance should be inserted later

Abstract The nonlinear dynamics of many under-actuated wheeled platforms are governed by nonholonomic constraints of no-skid for passively rolling wheels, coupled with momentum balance. In most of theoretical models, the shape variables, i.e. joint angles, are directly prescribed as periodic inputs, such as steering angle of the Twistcar. In this work, we study a variant of the Twistcar model where the actuation input is periodic oscillations of an inertial rotor attached to the main body, while the steering joint is passively free to rotate. Remarkably, the dynamics of this model is extremely rich, and includes multiplicity of periodic solutions, both symmetric and asymmetric, as well as stability transitions and bifurcations. We conduct numerical simulations as well as asymptotic analysis of the vehicle's reduced equations of motion. We use perturbation expansion in order to obtain leading-order dynamics under symmetric periodic solution. Then, we utilize harmonic balance and further scaling assumptions in order to approximate the conditions for symmetry-breaking pitchfork bifurcation and stability transition of the symmetric periodic solution, as a function of actuation frequency and structural parameters. The asymptotic results show good agreement with numerical simulations. The results highlight the role of passive shape variables in generating multi-stable periodic solutions for nonholonomic systems of robotic locomotion.

Keywords bifurcations, stability transition

1 Introduction

Many under-actuated wheeled platforms contain axles of passively rolling wheels. Examples are various skating boards such as snakeboard and carver board, as well as children's toy cars such as Twistcar. The dynamic motion of such platform is governed by enforcing zero lateral slip (i.e. skid) of the wheels, coupled with actuation of periodic inputs. No-skid constraints are nonholonomic in their nature [6,31], constraining the system's instantaneous allowable velocity directions, similar to ice-skating blades.

Early mathematical examples of nonholonomic systems included planar kinematic models of a car with controlled steering (Dubins' car [26]), or truck connected to a chain of passive wheeled trailers via hinged passive joints [28]. The inputs to such systems were kinematic – driving speed and prescribed steering angle or its angular velocities. The main challenges in such systems were planning a motion trajectory that respects all nonholonomic constraints [36], and feedback stabilization of tracking the desired path [45]. Another example is the three-wheel snake robot [41,46], which has three axles of passive wheels and two joint angles prescribed as periodic inputs (gaits). Such systems were analyzed utilizing concepts of geometric mechanics [22,33]. Other related models of three-link two-joint systems governed by first-order constraints on shape- and body-velocities are Purcell's swimmer in highly viscous flow [3], and inertial three-link swimmer in ideal fluid [20], which were analyzed using similar geometric tools [15,18].

In cases where the number of nonholonomic constraints is less than the number of passive degrees-of-freedom, the system is no longer “kinematic” and its motion is governed by coupling of momentum balance, nonholonomic constraints, and the periodic actuation. An early basic example of such dynamic-nonholonomic system is Chaplygin's sleigh [8,42], a planar passive rigid body with a point blade,

*Corresponding Author E-mail: annar@technion.ac.il

A. Z., Z. Y., R. L., and Y. O. are with the Faculty of Mechanical Engineering, Technion - Israel Institute of Technology, Haifa 3200003, Israel

which is allowed to move only in a specific body-fixed direction. Later works studied variants of Chaplygin's sleigh with different types of added oscillatory actuation [21, 32, 43], and also with incorporation of frictional energy dissipation [4, 12, 13]. Several theoretical works have studied skating and riding toys in the framework of underactuated robots, including snakeboard [35], tricycle [9] and several variants of the roller-racer [5, 24], which was also named Landshark [2] and Twistcar [7, 16]. Some of these works utilized concepts of geometric mechanics for analyzing the robot's net motion under oscillatory inputs [33, 34], whereas other works employed asymptotic analysis [7, 16] and other methods [1, 2]. Few of these works also included experiments with robotic prototypes [9, 23, 25, 40]. The periodic inputs of such robots and models commonly involve relative angles at joints connecting the links, such as two joint angles of the three-wheel snake [38, 41, 46] and a single steering joint angle of the roller-racer/Twistcar/Landshark [2, 7, 24]. Other options are an oscillating mass on top of the main body of Chaplygin's sleigh [32], and angular oscillations of an inertial rotor as in the "Chaplygin's Beanie" model [21], or in the snakeboard [35], whose rotor represents waist twisting motion of a human rider standing on the board.

In the models mentioned above, all shape variables, i.e. joint angles, are directly prescribed as inputs. In contrast, recent works have studied underactuated passive-wheeled multi-link robots such that at least one internal joint is passive. In most cases, these passive joints are acted by torsional spring and damper, representing structural visco-elasticity [10, 11]. This adds dynamic coupling of the internal shape variable with the body motion and periodic actuation, which often results in existence of optimum mean speed due to its non-monotonic dependence on frequency of the oscillatory input [38].

Importantly, recent theoretical works also found that incorporating passive visco-elastic shape variables may also introduce multiplicity of periodic motions, as well as their stability transitions and bifurcations. While these effects have been studied for multi-link swimmer models with internal [44, 47] or external actuation [17, 37], they were recently found also in the work [39], which considered a simple modification of Chaplygin sleigh model. The planar two-link model in [39] consists of a sleigh with a single no-skid blade, connected to a second link by a revolute joint with torsional spring and viscous damper, in parallel to periodic input of joint torque actuation. The work showed that one can tune the spring's potential elastic energy in order to induce existence of asymmetric fixed points of joint angle, leading to multiplicity of periodic solutions oscillating about those fixed points. Furthermore, these limit cycles may undergo stability transitions upon varying the input actuation frequency. The interesting results in [39] call for extension and exploration of other models of dynamic underactuated non-

holonomic systems with passive shape variables, as well as deeper investigation using asymptotic analysis.

In our current work, we study a variant of the planar Twistcar model in [7], called RAPS Twistcar (Rotor-Actuated Passive Steering Twistcar). The model, introduced in Section 2 below, consists of two links supported by two no-skid wheeled axles with rolling resistance of viscous dissipation, see Fig. 1. Inspired by the snakeboard [35], the actuation input is periodic oscillations of an inertial rotor attached to the main body, while the steering joint is passively free to rotate, with zero torque and no elasticity or friction. Remarkably, numerical simulations (Section 3) reveal that the dynamics of this model is extremely rich, and includes multiplicity of periodic solutions, both symmetric and asymmetric, as well as stability transitions and bifurcations. After simplifying reduction of the system's dynamic equations of motion in Section 4, we conduct in Section 5 numerical Poincaré map analysis [14] for numerically finding periodic solutions and examine their stability. This reveals bifurcations, stability transitions and symmetry-breaking of periodic solution branches. Next, in Section 6 we present asymptotic analysis of the vehicle's reduced equations of motion assuming small-amplitude oscillations of the input. We use perturbation expansion [29] to obtain the system's approximate leading-order dynamics under symmetric periodic solution, which enables finding optimal placement of the bod's center of mass. Finally, in Section 7 we utilize harmonic balance [30] and further scaling assumptions in order to approximate the conditions for symmetry-breaking pitchfork bifurcation and stability transition of the symmetric periodic solution, as a function of actuation frequency and structural parameters. The asymptotic results show good agreement with numerical simulations. Our results highlight the significant role of passive shape variables in generating multi-stable periodic solutions for nonholonomic systems of robotic locomotion, and the importance of asymptotic analysis for improved understanding of these intriguing phenomena.

2 Problem formulation

The simplified physical model of the RAPS-Twistcar is shown in Fig. 1. Like the Twistcar model [7], this system consists of two rigid links supported by wheeled axles: the longer link represents the rider and the body of the Twistcar, while the shorter link represents the steering lever controlling the front wheels. We denote the mass and inertia of the longer link by m_1 and I_1 , the body mass and inertia of the rider by m_r , I_r , and the mass and inertia of the frontal link by m_2 , I_2 . We assume that the front and rear wheels cannot skid sideways (no-skid conditions), which are introduced as nonholonomic constraints.

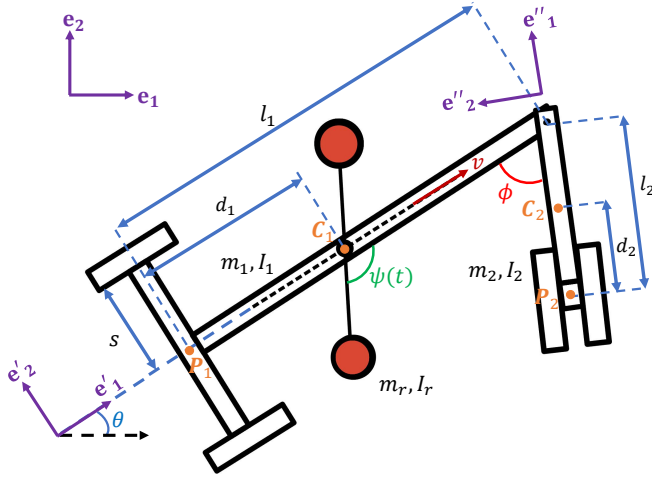


Fig. 1: The RAPS-Twistcar model.

The system's motion is described by \mathbf{q} , consisting of five generalized coordinates,

$$\mathbf{q} = (x, y, \theta, \phi, \psi)^T, \quad (1)$$

where (x, y) denote the position of the point P in world-fixed frame $\{\mathbf{e}_1, \mathbf{e}_2\}$, θ is the orientation angle of the body link of the car with respect to world frame, ϕ is the relative angle between the two links, and ψ is the relative angle between the rotor and the longer link. The rotor angle ψ is used as the input to the system,

$$\psi(t) = A \sin(\Omega t), \quad (2)$$

where A is the amplitude, t is time, and Ω is frequency. We define the x, y and θ as the body coordinates and ϕ as the shape variable.

The kinetic energy in this system may be expressed as,

$$E_K = \frac{1}{2}(m_1 + m_r)(\mathbf{v}_{C_1} \cdot \mathbf{v}_{C_1}) + \frac{1}{2}m_2(\mathbf{v}_{C_2} \cdot \mathbf{v}_{C_2}) + \frac{1}{2}I_1\dot{\theta}^2 + \frac{1}{2}I_2(\dot{\theta} + \dot{\phi})^2 + \frac{1}{2}I_r(\dot{\psi} + \dot{\theta})^2, \quad (3)$$

where \mathbf{v}_{C_i} is the velocity of point C_i , which is the center-of-mass (COM) of link i for $i = 1, 2$ (see Fig. 1).

The nonholonomic no-skid constraints can be expressed as $\mathbf{v}_{P_1} \cdot \mathbf{e}'_2 = 0$ and $\mathbf{v}_{P_2} \cdot \mathbf{e}''_2 = 0$, where $\{\mathbf{e}'_1, \mathbf{e}'_2\}$ frame is attached to the body link, $\{\mathbf{e}''_1, \mathbf{e}''_2\}$ frame is attached to the frontal link, and \mathbf{v}_{P_i} is the velocity of point P_i for $i = 1, 2$ (see Fig. 1). These constraints may be expressed in a matrix form, as

$$\mathbf{W}(\mathbf{q})\dot{\mathbf{q}} = 0, \quad \mathbf{W}(\mathbf{q}) = \begin{pmatrix} -\sin(\theta) & \cos(\theta) & 0 & 0 & 0 \\ -\sin(\phi + \theta) & \cos(\phi + \theta) & l_1 \cos(\phi) - l_2 & -l_2 & 0 \end{pmatrix}. \quad (4)$$

In order to add viscous rolling resistance to the model, we use Rayleigh's dissipation function, as follows. For each wheel, we define the velocity along its permissible roll direction using the Jacobian,

$$\mathbf{v}_{\parallel, i} = \mathbb{J}_i(\mathbf{q})\dot{\mathbf{q}}. \quad (5)$$

Using the Jacobian notation, we define Rayleigh's dissipation function,

$$\mathcal{R}(\mathbf{q}, \dot{\mathbf{q}}) = \frac{c}{2} \sum_{i=1}^3 \mathbf{v}_{\parallel, i}^T \mathbf{v}_{\parallel, i} = \frac{c}{2} \dot{\mathbf{q}}^T \left(\sum_{i=1}^3 \mathbb{J}_i(\mathbf{q})^T \mathbb{J}_i(\mathbf{q}) \right) \dot{\mathbf{q}}, \quad (6)$$

where c is the viscous damping coefficient.

We differentiate (6) with respect to the generalized velocity $\dot{\mathbf{q}}$ to obtain the dissipation contribution to the dynamic equations. Using the Jacobian notation, we obtain that

$$\mathbf{D}(\mathbf{q}, \dot{\mathbf{q}}) = \frac{\partial \mathcal{R}}{\partial \dot{\mathbf{q}}} = c \left(\sum_{i=1}^3 \mathbb{J}_i(\mathbf{q})^T \mathbb{J}_i(\mathbf{q}) \right) \dot{\mathbf{q}}. \quad (7)$$

Next, following [25], we derive the equations-of-motion of the system. More specifically, using the Euler-Lagrange formulation [27], with the assumption of a planar model with a constant potential energy, we obtain:

$$\mathbf{M}(\mathbf{q})\ddot{\mathbf{q}} + \mathbf{B}(\mathbf{q}, \dot{\mathbf{q}}) + \mathbf{D}(\mathbf{q}, \dot{\mathbf{q}}) = \mathbf{F}_q + \mathbf{W}^T(\mathbf{q})\boldsymbol{\Lambda}, \quad (8)$$

where $\mathbf{M}(\mathbf{q})$ is the system's matrix of inertia, $\mathbf{B}(\mathbf{q}, \dot{\mathbf{q}})$ is the vector of velocity-dependent inertial forces and $\mathbf{D}(\mathbf{q}, \dot{\mathbf{q}})$ is the vectors of dissipation forces. $\boldsymbol{\Lambda} = [\lambda_1 \ \lambda_2]^T$ is the vector of forces enforcing the constraints and $\mathbf{F}_q = [0 \ 0 \ 0 \ 0 \ \tau]^T$ is the vector of generalized forces, which includes the applying an outside torque τ on the rotor angle.

By differentiating (4) with respect to time, we get two more equations, which may be expressed as

$$\mathbf{W}(\mathbf{q})\ddot{\mathbf{q}} + \dot{\mathbf{W}}(\mathbf{q})\dot{\mathbf{q}} = 0. \quad (9)$$

3 Numerical simulations

The system of equations in (8)-(9) is differential-algebraic, which is possible to solve by numeric integration, for example by using "ode45" solver in Matlab. To simulate this system we use the parametric values in Table 1, where note that we neglect the mass and inertia of the vehicle's links with respect to the rotor, so that m_1 and m_2 are negligible with respect to m_r . Similarly, I_1 and I_2 are negligible with respect to I_r . Hence, hereafter we assume that $m_1 = m_2 = I_1 = I_2 = 0$. Note that although this assumption implies that the matrix \mathbf{M} is singular, the system of equations in (8)-(9) is non-singular, where $\psi(t)$ and its derivatives are known.

We hereby present results of various numerical simulations. In Fig. 2(a) we show the dependence of the passive

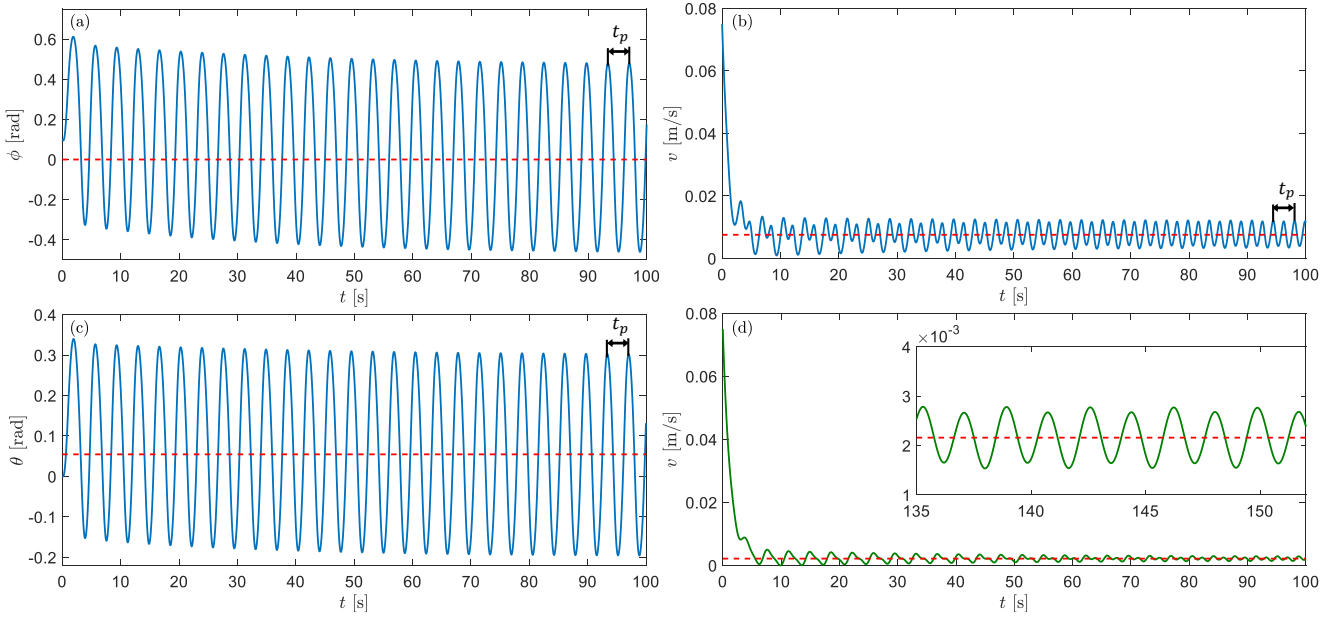


Fig. 2: Numerical simulation for “high” frequency $\Omega = 1.72$ [rad/s] resulting in convergence to a symmetric periodic solution, where the physical parameters are given in Table 1. (a) The passive steering angle ϕ versus time t . (b) The speed v in direction parallel to the main link versus time t . (c) The body orientation angle θ versus time t . (d) The speed v in direction parallel to the main link versus time t , for the parameter values as given in Table 1, except that now $d_1 = 0.12$ [m]. In the inset of (d) we show magnified view of the convergence to the steady-state. The steady-state mean values $\bar{\phi}$, \bar{v} , $\bar{\theta}$, and \bar{v} are indicated by red dashed lines in panels (a)-(d), respectively.

Parameter	Value	Description
l_1	0.6 [m]	main body length
l_2	0.2 [m]	frontal link length
d_1	0.06 [m]	main body COM location
d_2	0.1 [m]	frontal link COM location
s	0.2 [m]	rear wheels width
m_r	40 [kg]	rotor mass
I_r	0.1695 [kg·m ²]	rider inertia
c	10 [N·s/m]	rolling dissipation coefficient
A	1 [rad]	actuation amplitude

Table 1: Dimensions and values of the model’s physical parameters.

joint angle ϕ on time t . We used the parameters from Table 1 and assumed that the actuation of the simulation is $\psi(t) = A \sin(\Omega t)$, with the amplitude of $A = 1$ [rad] and frequency $\Omega = 1.72$ [rad/s]. The solution is composed of an initial transient which converges to a steady-state periodic solution. It is possible to see that $\phi(t)$ converges to a periodic signal with frequency which equals to the actuation frequency.

Let us define the mean value $\bar{\phi}$ about which the angle $\phi(t)$ oscillates as the mean over a period, after initial transient response followed by convergence to the periodic solution for ϕ . Similarly, we define the mean values $\bar{\theta}$ and \bar{v} ,

namely

$$\bar{\phi} = \frac{1}{t_p} \int_{t_0}^{t_0+t_p} \phi(t) dt, \quad \bar{\theta} = \frac{1}{t_p} \int_{t_0}^{t_0+t_p} \theta(t) dt, \quad (10)$$

$$\bar{v} = \frac{1}{t_p} \int_{t_0}^{t_0+t_p} v(t) dt,$$

where $t_p = 2\pi/\Omega$ denotes the period of the actuation $\psi(t)$ and t_0 is an arbitrary time after reaching the steady-state behavior. For the simulation shown in Fig. 2(a), $\bar{\phi} = 0$ is indicated by red dashed line. This means that the steady-state periodic solution is *symmetric* relative to the main body link.

We define the velocities v_{\parallel} and v_{\perp} as the velocity components of point P_1 along \mathbf{e}_1' and \mathbf{e}_2' directions, respectively, and for brevity denote $v = v_{\parallel}$. In Fig. 2(b), we show the speed v of the twist-car robot versus time t . It can be seen that after an initial transient the frequency of the periodic function $v(t)$ becomes doubled relative to the frequency of the actuation $\psi(t)$. Moreover, the steady-state function $v(t)$ oscillates about a constant $\bar{v} \neq 0$, which is indicated by red dashed line in Fig. 2(b). In Fig. 2(c), we show the passive angle θ versus time t . It can be observed that after the initial transient the passive angle $\theta(t)$ oscillates about a constant value $\bar{\theta} \neq 0$. In Fig. 2(d), we show the speed $v(t)$ for the parameter values from Table 1, except that now the parameter d_1 is doubled, $d_1 = 0.12$ [m]. It can be observed that the value of d_1 has a significant effect on the average speed \bar{v} ,

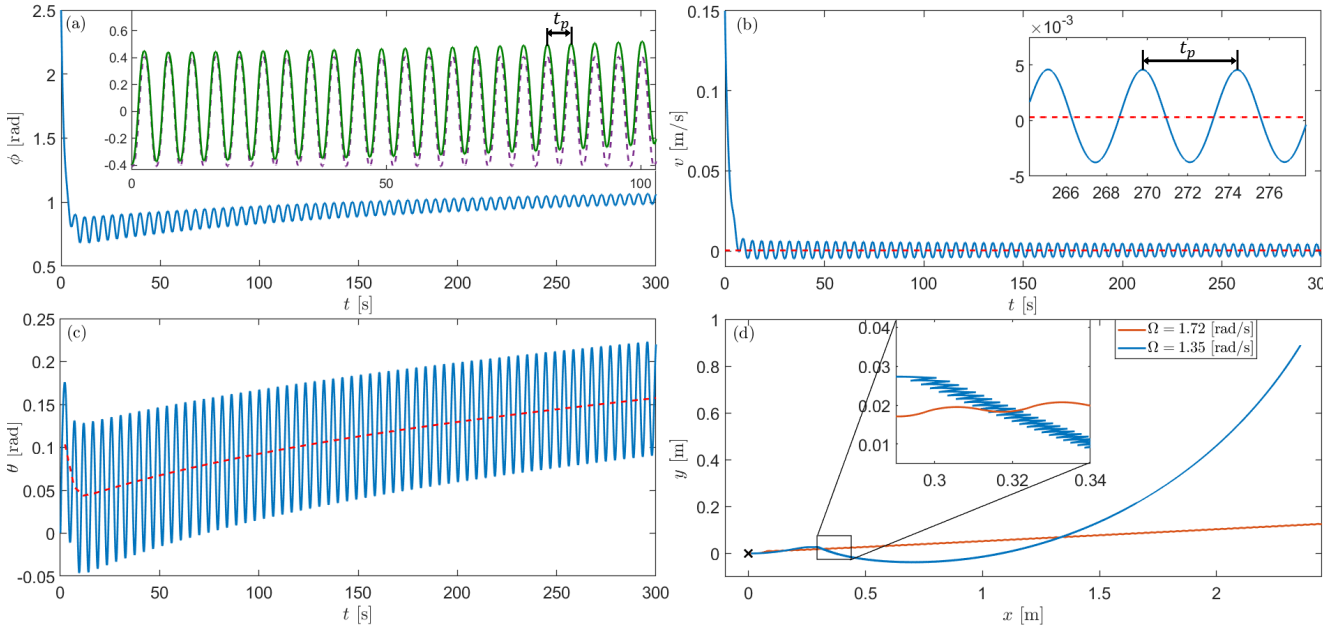


Fig. 3: Numerical simulation for “low” frequency $\Omega = 1.35$ [rad/s], where the physical parameters are given in Table 1. (a) The passive steering angle ϕ versus time t , which converges to asymmetric periodic solution, where in the inset we show an unstable symmetric solution with ‘exact’ initial conditions (purple dashed curve) and with slightly perturbed initial conditions (green curve). (b) The speed v in direction parallel to the main link versus time t , where its steady-state mean value \bar{v} is indicated by a red dashed line. In the inset we show a magnified view of (b) near the final time of the simulation. (c) The body orientation angle θ versus time t , where its mean value $\bar{\theta}$ over a period is indicated by a red dashed line. (d) Comparison between the trajectories in the xy -plane in the asymmetric case (blue curve) with the frequency of $\Omega = 1.35$ [rad/s] (as in the rest of the panels in this figure) and the symmetric case (orange curve) with the frequency of $\Omega = 1.72$ [rad/s] (as in Fig. 2), where in the inset we show a magnified view of (d) in the vicinity of the initial position, which is marked with ‘x’.

namely when decreasing d_1 from $d_1 = 0.12$ [m] (as shown in Fig. 2(d)) to $d_1 = 0.06$ [m] (as shown in Fig. 2(b)) the mean speed increases from about $\bar{v} \approx 2 \cdot 10^{-3}$ [m/s] to about $\bar{v} \approx 0.01$ [m/s]. We will further discuss the effect of d_1 on the mean speed of the steady-state symmetric periodic solution in Section 6.

In Fig. 3 we show a temporal simulation for the parameter values from Table 1, but for a lower frequency of $\Omega = 1.72$ [rad/s]. In Fig. 3(a) we show the dependence of the passive joint angle ϕ on time t . The solution is composed of the initial transient which converges to a periodic solution. Remarkably, unlike the previous case in Fig. 2, $\bar{\phi}$, which was defined in (10) does not vanish here, but its value is $\bar{\phi} \approx 1.0343$ [rad]. This means that the periodic solution is *asymmetric* for this set of parameter values. In the inset of Fig. 3(a) we show that by choosing different initial conditions it is possible to obtain in this case a symmetric solution as well (shown by dashed purple curve). However, a small deviation from these initial conditions yields a solution (shown by a solid green curve) which initially stays close to the symmetric solution, but then leaves the symmetric solution and after a sufficiently long time it converges

to the asymmetric solution shown in panel (a). Thus, in this case the symmetric solution is *unstable*, whereas the asymmetric solution is *stable*.

In Fig. 3(b) we show the evolution in time of the forward speed $v(t)$. It can be seen that after the initial transient the speed converges to a periodic function with non-vanishing mean \bar{v} (marked by a red dashed line) but, contrary to the previous case, its frequency is equal to the frequency of the actuation function $\psi(t)$. In Fig. 3(c) we show the dependence of the angle θ on time t . It can be observed that it converges to a function whose mean $\bar{\theta}(t)$ (marked by a red dashed line) is a linear increasing function of t . This means that the vehicle has nonzero net rotation during its forward motion.

In Fig. 3(d) we show the solution trajectory in the xy -plane in two cases: the frequency of $\Omega = 1.35$ [rad/s] (as in the rest of panels in Fig. 3) and the frequency of $\Omega = 1.72$ [rad/s] (as in Fig. 2). The initial position in both cases is the same and it is marked with ‘x’. It is possible to see that while in the symmetric case after an initial transient the net motion of the Twistcar is along a straight line, in the asymmetric

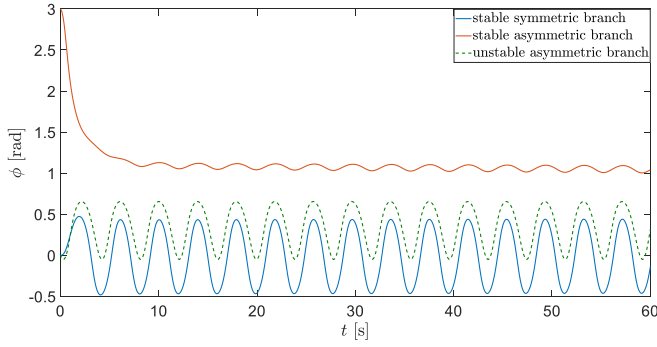


Fig. 4: Numerical simulation for “intermediate” frequency $\Omega = 1.6$ [rad/s] resulting in convergence to either a stable symmetric periodic solution (marked by a solid blue curve) or a stable asymmetric periodic solution (marked by a solid orange curve) depending on the initial conditions, where the physical parameters are given in Table 1. There also exists an unstable asymmetric periodic solution (marked by a dashed green curve), which is obtained for appropriate initial conditions. In all three cases we show the passive angle ϕ versus time t .

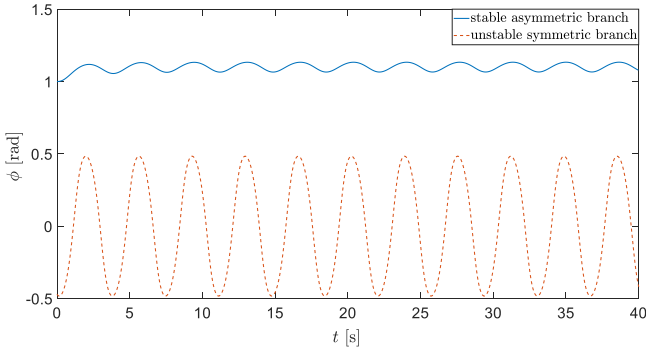


Fig. 5: Numerical simulation for “high” frequency $\Omega = 1.72$ [rad/s], which is the same case as for Fig. 2 except that now $d_1 = 0.04$ [m], where the rest of physical parameters are given in Table 1. The passive angle ϕ versus time t in two cases: convergence to a stable asymmetric periodic solution with $\bar{\phi} \neq 0$ (shown by solid blue curve) and an unstable symmetric periodic solution with $\bar{\phi} = 0$ (shown by dashed orange curve).

case after an initial transient the net motion of the Twistcar is along a circular arc.

Since in the case of “high” frequency $\Omega = 1.72$ [rad/s] (as shown in Fig. 2) the simulation converges to a symmetric solution and in the case of “low” frequency $\Omega = 1.35$ [rad/s] (as shown in Fig. 3) the simulation converges to an asymmetric solution, in Fig. 4 we show the dependence of the passive joint angle ϕ on time t for an intermediate frequency of $\Omega = 1.6$ [rad/s], where the rest of parameter values are the same as previously (as given in Table 1). It can be seen that

in this case the simulation may converge to either a stable symmetric periodic solution or a stable asymmetric periodic solution depending on the initial conditions. Moreover, in this case there exists also an unstable asymmetric periodic solution, which is obtained when the initial conditions are chosen appropriately. Thus, we may conclude that the value of frequency Ω affects the existence of stable/unstable symmetric and asymmetric periodic solutions.

An interesting question which arises in view of the results shown in Figs. 2–4 is if only the value of frequency Ω affects the existence of stable/unstable symmetric and asymmetric periodic solutions or any other parameter values, say the location of rotor’s COM d_1 , may also affect this issue. To answer this question, we show in Fig. 5 the dependence of ϕ on time t for the same frequency, of $\Omega = 1.72$ [rad/s], and the same physical parameters as in Fig. 2 (see Table 1), except d_1 which is now $d_1 = 0.04$ [m]. While in Fig. 2 we obtain convergence to a symmetric periodic solution, in Fig. 5 we show convergence to an asymmetric periodic solution, where also an unstable symmetric periodic solution does exist and may be obtained with an appropriate choice of the initial conditions. Hence, our conclusion is that also the location of rotor’s COM d_1 affects the existence of stable/unstable symmetric and asymmetric periodic solutions.

We have found numerically that this nonlinear system has many interesting dynamical phenomena of multiplicity of periodic solutions, and changes of their properties depending on actuation frequency and other parameters. The aim of the following sections is to formulate these phenomena analytically, using asymptotic approximations.

4 Reduction of the system’s dynamics

Here we present reorganization of the equations of motion in a more reduced form. First, we transform the generalized velocities to body-frame velocities $\mathbf{v}_b = [v_{\parallel} \ v_{\perp} \ \dot{\theta} \ \dot{\phi} \ \dot{\psi}]^T$, using the transformation matrix \mathbf{R}_b , as follows

$$\mathbf{v}_b = \mathbf{R}_b(\theta)^T \dot{\mathbf{q}}, \text{ where } \mathbf{R}_b(\theta) = \begin{bmatrix} \cos(\theta) & -\sin(\theta) & 0 & 0 & 0 \\ \sin(\theta) & \cos(\theta) & 0 & 0 & 0 \\ 0 & 0 & 1 & 0 & 0 \\ 0 & 0 & 0 & 1 & 0 \\ 0 & 0 & 0 & 0 & 1 \end{bmatrix}. \quad (11)$$

Expressing the constraints in (4) in terms of the body-frame velocities \mathbf{v}_b , we have that

$$\mathbf{W}\dot{\mathbf{q}} = \underbrace{(\mathbf{W}\mathbf{R}_b)}_{\mathbf{W}_b} \underbrace{(\mathbf{R}_b^{-1}\dot{\mathbf{q}})}_{\mathbf{v}_b} = \begin{bmatrix} 0 & 1 & 0 & 0 & 0 \\ -\sin\phi & \cos\phi & l_1\cos\phi - l_2 & -l_2 & 0 \end{bmatrix} \begin{bmatrix} v_{\parallel} \\ v_{\perp} \\ \dot{\theta} \\ \dot{\phi} \\ \dot{\psi} \end{bmatrix} = \mathbf{0}. \quad (12)$$

Next, we reduce the number of the body-frame velocities to the vector of 3 unknowns $\mathbf{v}_r = [v_{\parallel} \ \dot{\theta} \ \dot{\psi}]^T$. Note that the skid velocity of point P_1 , v_{\perp} , is identically zero according to our definition and the non-holonomic constraints. Hence, the transformation from the reduced velocities \mathbf{v}_r to body-frame velocities \mathbf{v}_b may be expressed as,

$$\mathbf{v}_b = \mathbf{S}_r \mathbf{v}_r, \quad \text{where} \quad \mathbf{S}_r = \begin{bmatrix} 1 & 0 & 0 \\ 0 & 0 & 0 \\ 0 & 1 & 0 \\ -\frac{\sin\phi}{l_2} & \frac{l_1}{l_2}\cos\phi - 1 & 0 \\ 0 & 0 & 1 \end{bmatrix}. \quad (13)$$

Note that body-frame velocities \mathbf{v}_b in (13) automatically satisfy the nonholonomic constraints in (12). From the transformation in (11) and the reduction in (13), we obtain a relation between the generalized velocities and the reduced body velocities, $\dot{\mathbf{q}} = \mathbf{S} \mathbf{v}_r$, where the transformation matrix is given by $\mathbf{S} = \mathbf{R}_b \mathbf{S}_r$. Substituting this relation between generalized and reduced velocities into (8), we obtain the reduced equation

$$\mathbf{M}_r(\phi) \dot{\mathbf{v}}_r + \mathbf{B}_r(\phi, \mathbf{v}_r) + \mathbf{D}_r(\phi, \mathbf{v}_r) = \mathbf{F}_r, \quad (14)$$

where

$$\mathbf{M}_r(\phi) = \mathbf{S}^T \mathbf{M} \mathbf{S} \in \mathbb{R}^{3 \times 3},$$

$$\mathbf{B}_r(\phi, \mathbf{v}_r) = \mathbf{S}^T \mathbf{M} \dot{\mathbf{S}} \mathbf{v}_b + \mathbf{S}^T \mathbf{B} \in \mathbb{R}^{3 \times 1}, \quad \mathbf{F}_r = [0 \ 0 \ \tau]^T,$$

and where $\mathbf{D}_r = \mathbf{S}^T \mathbf{D}(\mathbf{q}, \dot{\mathbf{q}})$, after substituting the velocity relations (11) and (13). Detailed expressions for \mathbf{M}_r , \mathbf{B}_r , and \mathbf{D}_r appear in Appendix A, equations (A.1)-(A.3).

Next, we express the equations in (14) and the constraints in (12) in a more concise way. We start by using the first constraint in (12), according to which v_{\perp} vanishes. Hence, for brevity, we denote $v = v_{\parallel}$. Note that in this case the system in (14) contains three equations, where the last equation is decoupled from the rest. Since $\psi(t)$ is a given function of time, the dynamics of the system is governed by the first two equation in (14), whereas the third equation contains the

actuation torque τ . Thus, the system in (14) reduces to the following two equations in three unknowns $(v, \dot{\theta}, \phi)$,

$$m_r \dot{v} - d_1 m_r \dot{\theta}^2 + c \left[(2 + \cos^2(\phi))v + \frac{l_1}{2} \sin(2\phi) \dot{\theta} \right] = 0, \quad (15a)$$

$$(I_r + d_1^2 m_r) \ddot{\theta} + I_r \ddot{\psi} + d_1 m_r v \dot{\theta} + c \left[\frac{l_1}{2} v + (2d^2 + l_1^2 \sin^2(\phi)) \dot{\theta} \right] = 0. \quad (15b)$$

The third equation is obtained from the second constraint in (12), which yields that

$$\dot{\phi} = -\frac{1}{l_2} v \sin\phi + \dot{\theta} \left(\frac{l_1}{l_2} \cos\phi - 1 \right). \quad (15c)$$

Next, to render the problem in (15) dimensionless, we first define $t_c = m_r/c$ as the characteristic time scale of the problem with c denoting the rolling dissipation coefficient. Then, all time-dependent quantities are scaled as

$$\begin{aligned} \tilde{v} &= \frac{t_c}{l_1} v, \quad \tilde{\dot{v}} = \frac{d\tilde{v}}{d\tilde{t}} = \frac{t_c^2}{l_1} \dot{v}, \quad \tilde{\dot{\theta}} = t_c \dot{\theta}, \quad \tilde{\ddot{\theta}} = t_c^2 \ddot{\theta}, \\ \tilde{\dot{\phi}} &= t_c \dot{\phi}, \quad \tilde{\ddot{\psi}} = t_c^2 \ddot{\psi}, \quad \tilde{t} = \frac{t}{t_c}, \quad \tilde{\omega} = t_c \Omega. \end{aligned} \quad (16)$$

For convenience, we define the following dimensionless parameters,

$$\alpha = \frac{s}{l_1}, \quad \beta = \frac{l_2}{l_1}, \quad \delta = \frac{d_1}{l_1}, \quad \eta = \frac{I_r}{m_r l_1^2}, \quad (17)$$

and hereafter remove the tilde (\sim) symbol from all of the variables, where we use the convention that they represent scaled dimensionless quantities.

Finally, substituting (16) and (17) into the system in (15) and denoting for brevity $\sigma = \dot{\theta}$, we obtain the following dimensionless system of nonlinear ODEs,

$$\dot{\mathbf{z}} = \begin{pmatrix} \frac{1}{\beta} [-v \sin(\phi) + (-\beta + \cos(\phi)) \sigma] \\ -\frac{[2\eta \ddot{\psi} + v \sin(2\phi) + (\alpha_1 - \cos(2\phi) + 2\delta v) \sigma]}{2(\delta^2 + \eta)} \\ \delta \sigma^2 - 0.5 \sigma \sin(2\phi) - 0.5(5 + \cos(2\phi))v, \end{pmatrix} \quad (18)$$

where $\alpha_1 = 1 + 4\alpha^2$, $\mathbf{z} = (\phi, \sigma, v)^T$ and $\ddot{\psi} = -A\omega^2 \sin(\omega t)$.

5 Analysis of periodic solutions

In this section, we investigate periodic solutions and their stability by using the Poincaré map [14]. The methodology for finding and analyzing the periodic solutions is as follows. Note that in (18), the vector $\mathbf{z} = (\phi, \sigma, v)^T$ describes the system's solution. Next, we define $\mathbf{z}_k = \mathbf{z}(t = kt_p)$, $k = 0, 1, 2, \dots$, where $t_p = 2\pi/\omega$ is the nondimensional period

time. Since the actuation is periodic in t_p , it is possible to express the discrete dynamic equation, without time dependency, as

$$\mathbf{z}_{k+1} = \mathbf{P}(\mathbf{z}_k), \quad (19)$$

where \mathbf{P} denotes the Poincaré map of the system, see [14] for further details. More specifically, we refer here to Poincaré stroboscopic map due to the use of the actuation's period as the sampling time interval. It is possible to evaluate $\mathbf{P}(\mathbf{z}_k)$ by numeric integration of (18) over a period. Since a periodic solution of (18) satisfies $\mathbf{z}(t) = \mathbf{z}(t + t_p)$, in order to find it one needs to solve the system $\mathbf{P}(\mathbf{z}^*) = \mathbf{z}^*$. We find solution of \mathbf{z}^* numerically, by using 'fsolve' function in Matlab.

The stability of a periodic solution is determined via the eigenvalues λ_i of the linearization matrix

$$\mathbf{J} = \left. \frac{d\mathbf{P}}{d\mathbf{z}} \right|_{(\mathbf{z}=\mathbf{z}^*)}. \quad (20)$$

Specifically, a periodic trajectory is asymptotically stable if and only if all of the eigenvalues, called Floquet multipliers [14], satisfy $|\lambda_i| < 1$. It is possible to estimate the matrix \mathbf{J} by numerical differentiation of \mathbf{P} . Thus, by using Poincaré map it is possible to find periodic solutions and assess their stability.

In Fig. 6 we show multiplicity of the periodic solutions and their stability obtained by using Poincaré map. More specifically, in Fig. 6(a) we show the mean angle $\bar{\phi}$ versus frequency ω for parameter values given in Table 1, where solid curves indicate stable solutions and dashed curves indicate unstable solutions. It can be seen that for sufficiently small ω , $\omega < 6.03$, there exist two stable asymmetric solutions and an unstable symmetric solution. Then, at $\omega = 6.03$ there exists a *pitchfork bifurcation*, where the symmetric solution becomes stable and two additional asymmetric branches, which are unstable, emerge. At $\omega = 6.81$ there exists an additional bifurcation, known as *fold bifurcation*, which means that the two stable asymmetric solutions exist for $\omega < 6.81$ and the two unstable asymmetric solutions exist for $6.03 < \omega < 6.81$. Note that all values are truncated to two significant digits.

In Fig. 6(b) we show the mean angle $\bar{\phi}$ versus the scaled rotor's COM position $\delta = d_1/l_1$, for $\omega = 6.88$ and the rest of parameter values as given in Table 1. It can be seen when the parameter δ is varied, there also exists a pitchfork bifurcation at $\delta \approx 0.0735$, where the symmetric periodic solution loses its stability and two additional unstable asymmetric periodic solutions emerge. Moreover, there also exists a fold-bifurcation at $\delta \approx 0.098$, which distinguishes between the ranges of existence and non-existence of asymmetric solutions.

In Figs. 6(c) and (d) we show the mean speed \bar{v} versus ω and δ for that same parameter values as in In Figs. 6(a) and (b), respectively. It is possible to observe that the mean

speed of the symmetric periodic solution is always greater or equal (at the bifurcation point) than the corresponding mean speed of the asymmetric periodic solution. Moreover, while the mean speed of the symmetric periodic solution is monotonically increasing with the frequency ω , it has an optimal value as a function of δ . Therefore, there exists an optimal position for the rotor's COM, which is approximately 20% of the main body length from the rear link, which yields the maximal mean forward speed.

In Fig. 7 we show the stability transition diagram for the symmetric periodic solutions in the $(\delta\omega)$ -plane. The curve in the figure was obtained numerically by using Poincaré map and the bisection method. More specifically, for any fixed δ , by modifying the values of ω , we follow the symmetric periodic solution and calculate its Floquet multipliers. To obtain the stability transition point we use the bisection method, which allows us to find ω corresponding to the point where the maximal eigenvalue magnitude crosses 1. We repeat this procedure for a discrete sequence of values of δ in the desired interval.

As shown in Fig. 7, the symmetric periodic solution is stable above the stability transition curve, and unstable below it. Moreover, it can be seen that the stability transition curve may be expressed via a function of bifurcation frequency ω versus δ , which is monotonically decreasing. One of our aims in the coming sections is to derive a closed-form polynomial which will approximate this stability transition curve.

6 Asymptotic analysis of symmetric periodic solution

We now present asymptotic analysis of symmetric periodic solution of the problem in (18). Under the assumption of sufficiently small A , η , and ω , let us define a small parameter $0 < \varepsilon = A\eta\omega^2 \ll 1$. Thus, we assume the following expansions

$$\begin{aligned} \phi(t) &= \phi_0(t) + \varepsilon\phi_1(t) + O(\varepsilon^2), \\ \sigma(t) &= \sigma_0(t) + \varepsilon\sigma_1(t) + O(\varepsilon^2), \\ v(t) &= v_0(t) + \varepsilon v_1(t) + \varepsilon^2 v_2(t) + O(\varepsilon^3). \end{aligned} \quad (21)$$

Note that $\phi_0(t) = \sigma_0(t) = v_0(t) = 0$, because when there is no actuation the solution is identically zero.

To find the first-order correction, we start from the second equation in (18), which leads at order $O(\varepsilon)$, to

$$\dot{\sigma}_1 = \frac{\sin(\omega t)}{\delta^2 + \eta} - q\sigma_1, \quad \text{where} \quad q = \frac{2\alpha^2}{\delta^2 + \eta}. \quad (22)$$

The general solution of (22) is given by

$$\begin{aligned} \sigma_1(t) &= e^{-qt} \left[\frac{\omega}{(\delta^2 + \eta)(q^2 + \omega^2)} + C \right] \\ &\quad + \frac{\omega \cos(\omega t) - q \sin(\omega t)}{(\delta^2 + \eta)(q^2 + \omega^2)}. \end{aligned} \quad (23)$$

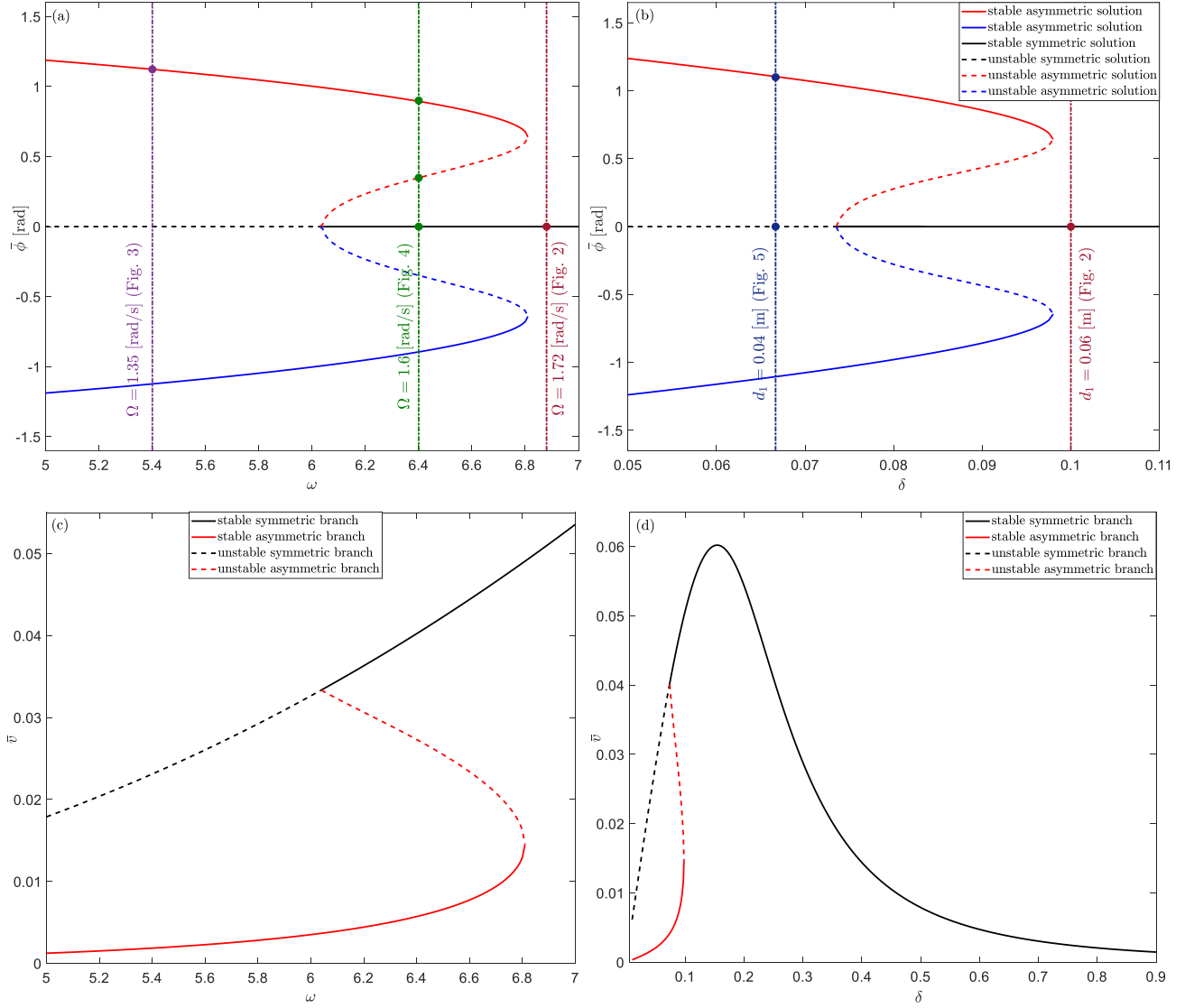


Fig. 6: Effects of nondimensional frequency and rotor's COM location on periodic solutions' properties, additional asymmetric solution branches, and bifurcations. Parameter values are given in Table 1 and nondimensional scaling in (17). (a) Mean angle $\bar{\phi}$ versus frequency ω . (b) Mean angle $\bar{\phi}$ versus rotor's COM location δ for frequency of $\omega = 6.88$. The three dashed-dotted vertical lines in panel (a) correspond to the results shown in Figs. 2–4 and the two dashed-dotted vertical lines in panel (b) correspond to Figs. 2 and 5. (c) Mean speed \bar{v} versus frequency ω . (d) Mean speed \bar{v} versus rotor's COM location δ for frequency of $\omega = 6.88$. The legend in panel (b) refers to both panels (a)-(b).

The first term in (23) decays exponentially in time and thus in steady-state the periodic solution may be expressed as,

$$\sigma_1(t) = b_1 \sin(\omega t) + b_2 \cos(\omega t), \quad (24)$$

where we define for brevity

$$b_1 = \frac{q}{(\delta^2 + \eta)(q^2 + \omega^2)}, \quad b_2 = -\frac{\omega}{(\delta^2 + \eta)(q^2 + \omega^2)}. \quad (25)$$

Substituting the solution in (24) into the first equation in (18), we obtain:

$$\dot{\phi}_1(t) = \frac{1-\beta}{\beta} \sigma_1(t), \quad (26)$$

which yields that the steady-state symmetric solution is given by,

$$\phi_1(t) = a_1 \sin(\omega t) + a_2 \cos(\omega t), \quad (27)$$

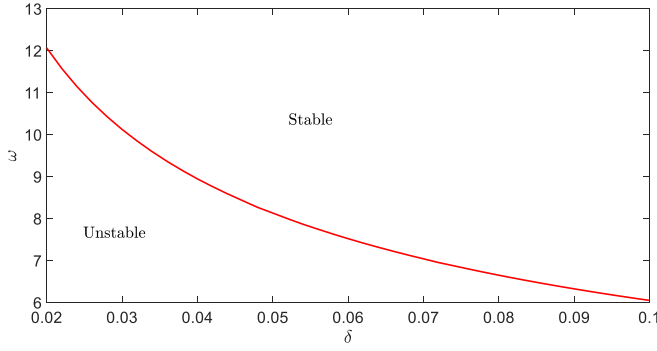


Fig. 7: Stability transition curve for the symmetric periodic solution. The bifurcation frequency ω versus rotor's COM location δ , for the parameter values given in Table 1 and nondimensional scaling in (17).

where we define for brevity

$$a_1 = \frac{(\beta - 1)}{\beta(q^2 + \omega^2)(\delta^2 + \eta)}, \quad a_2 = \frac{q(\beta - 1)}{\beta\omega(q^2 + \omega^2)(\delta^2 + \eta)}. \quad (28)$$

The expressions for $\phi_1(t)$ and $\sigma_1(t)$ are then substituted into the third equation in (18), and we obtain at order $O(\varepsilon)$ that $\dot{v}_1(t) = -3v_1(t)$. Hence, $v_1(t) = 0$ in steady-state after the transient response has decayed. Thus, expanding up to order $O(\varepsilon^2)$, we obtain that

$$v_1(t) = 0, \quad \dot{v}_2 = \delta\sigma_1^2 - \sigma_1\phi_1 - 3v_2. \quad (29)$$

Solving this equation we obtain that, in steady-state after the transient response has decayed, the solution is given by

$$v_2(t) = c_0 + c_1 \sin(2\omega t) + c_2 \cos(2\omega t), \quad (30)$$

where we define for brevity

$$c_1 = \frac{3q_1 + 2q_2\omega}{9 + 4\omega^2}, \quad c_2 = \frac{3q_2 - 2q_1\omega}{9 + 4\omega^2}, \quad (31)$$

where

$$c_0 = (\delta b_1^2 - a_1 b_1 + \delta b_2^2 - a_2 b_2)/6,$$

$$q_1 = \delta b_1 b_2 - 0.5(a_2 b_1 + a_1 b_2),$$

$$q_2 = 0.5(\delta b_2^2 - a_2 b_2 + a_1 b_1 - \delta b_1^2).$$

It is easy to verify by substituting a_i from (28) and b_i from (25), that that c_0 may be expressed as

$$c_0 = \frac{\delta}{6[4\alpha^4 + (\delta^2 + \eta)^2\omega^2]}. \quad (32)$$

Note that from (30) it follows that $\bar{v}_2 = c_0$, and hence the leading-order approximation for the mean speed is given by

$$\begin{aligned} \bar{v} &= \varepsilon^2 c_0 + O(\varepsilon^3) \\ &= \frac{A^2 \eta^2 \omega^4 \delta}{6[4\alpha^4 + (\delta^2 + \eta)^2 \omega^2]} + O(\varepsilon^3). \end{aligned} \quad (33)$$

When considering this expression as a function of δ , it is possible to conclude that \bar{v} attains at most one maximum (in the physically meaningful range $0 < \delta < 1$), which is located at

$$\delta_{\text{opt}} = \sqrt{\frac{\sqrt{12\alpha^4 + 4\eta^2\omega^2}}{3\omega} - \frac{\eta}{3}}. \quad (34)$$

Thus, the maximal mean speed is

$$\bar{v}_{\text{max}} = \frac{A^2 \eta^2 \omega^4 \delta_{\text{opt}}}{6[4\alpha^4 + (\delta_{\text{opt}}^2 + \eta)^2 \omega^2]}. \quad (35)$$

In Fig. 8(a,b) we show a comparison between numerical and asymptotic results calculated by using the approximate formula in (33) for the mean speed \bar{v} versus frequency ω for $\delta = 0.1$, and versus δ for $\omega = 6.88$, respectively. The rest of physical parameters are given in Table 1, except for the actuation amplitude which is $A = 0.5$. It can be seen that in both cases there is a very good agreement between numerical and asymptotic results, which will become even better upon decreasing the value of A .

In Fig. 9(a) we show a comparison between numerical and asymptotic results calculated by using the formula in (34) for δ_{opt} versus ω , for the parameter values given in Table 1 and three values of actuation amplitude A . Note that while the asymptotic expression for δ_{opt} is independent of A , the numerically calculated δ_{opt} depends on A . As A (and thus ε) decreases, the numerical results get closer to the asymptotic ones, so that for $A = 0.1$ they nearly coincide. According to the results shown in the graph, δ_{opt} is a monotonically decreasing function of ω , which means that in order to obtain optimal speed for higher frequency, one needs to move the rotor's COM closer to the rear wheels (see Fig. 1).

In Fig. 9(b) we show a comparison between numerical and asymptotic results calculated by using the formula in (35) for \bar{v}_{max}/A^2 versus ω , for the parameter values given in Table 1 and three values of A . It is possible to see that the agreement between the numerical and asymptotic results gets better as A and ω decrease, since ε is proportional to $A\omega^2$. In particular, for $A = 0.1$ the numerical and asymptotic results nearly coincide.

The comparison between numerical and asymptotic results demonstrates that the asymptotic analysis performed in this section provides a good approximation for the symmetric periodic solution. However, asymptotic analysis alone cannot capture the stability transition of the symmetric periodic solution, and thus in the next section we shall develop a methodology that allows to achieve this.

7 Bifurcations analysis of periodic solutions

In this section we derive an analytic approximation for a stability transition condition of the symmetric periodic so-

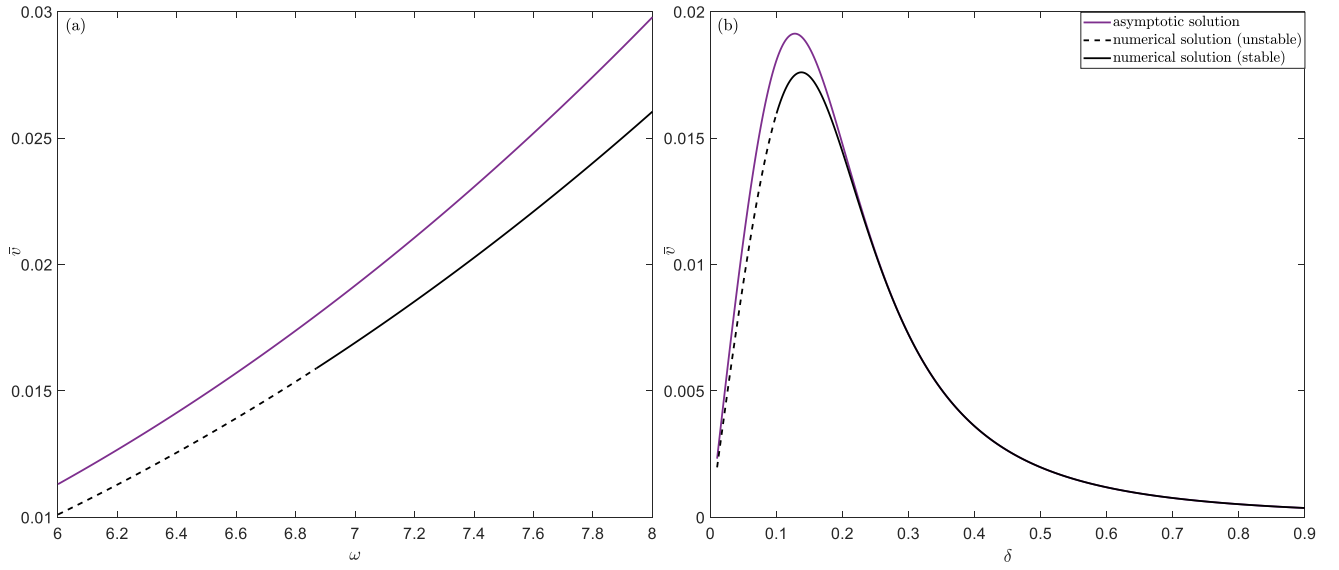


Fig. 8: Comparison between asymptotic (purple curve) and numerical (black curve) results for (a) mean speed \bar{v} versus frequency ω and (b) mean speed \bar{v} versus rotor's COM location δ . The dashed and solid black curves correspond to the unstable and stable symmetric periodic solutions, respectively. The parameter values are as given in Table 1 and nondimensional scaling in (17), except the amplitude A , which is now $A = 0.5$, and where in (b) $\omega = 6.88$.

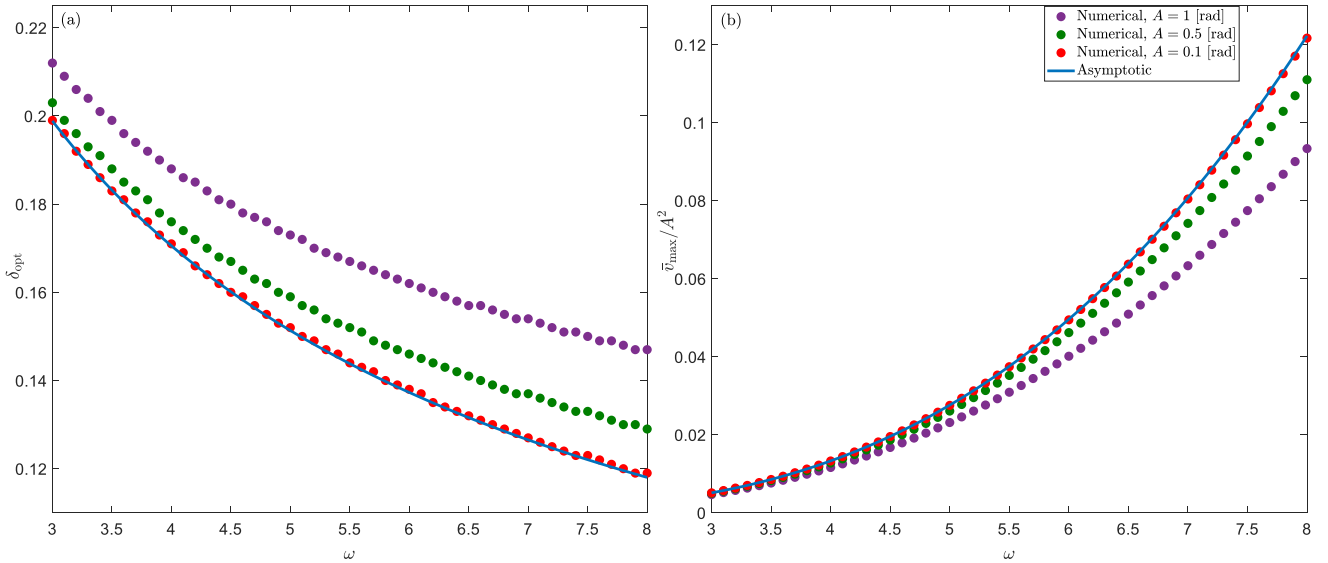


Fig. 9: Comparison between asymptotic (solid blue curve) and numerical (red, green, and purple circles) results for (a) optimal rotor's COM location δ_{opt} versus frequency ω and (b) optimal mean speed scaled by A^2 , namely \bar{v}_{max}/A^2 versus frequency ω . The physical parameter values are as given in Table 1 and nondimensional scaling in (17), except the amplitude A , which is now $A \in \{0.1, 0.5, 1\}$. The asymptotic results in (a) and (b) were obtained according to (34) and (35), respectively.

lution, where the methodology is based on harmonic balance [30].

Note that if we consider the asymptotic expansions of the steady-state solution for $0 < \varepsilon \ll 1$, which are given in (21) in Section 6, it is possible to obtain the epsilon-order of all terms in the equations in (18). More speci-

cally, the leading-order terms in the first and second equations in (18) are of order $O(\varepsilon)$, whereas the leading-order terms in the third equation in (18) are of order $O(\varepsilon^2)$. Thus, considering the leading-order equation resulting from the second equation in (18), we conclude that the term $2\delta v \sigma$ may be neglected, since it is of higher order $O(\varepsilon^3)$, assum-

ing $\delta = O(1)$. Neglecting the term $2\delta v\sigma$ in the second equation in (18) and multiplying the result by $2(\delta^2 + \eta)$, gives that

$$2(\delta^2 + \eta)\dot{\sigma} = -[(2\eta\dot{\psi} + v\sin(2\phi)) + (1 + 4\alpha^2 - \cos(2\phi))\sigma]. \quad (36)$$

Next, we multiply the first equation in (18) by $2\beta\cos(\phi)$, which yields that

$$2\beta\dot{\phi}\cos(\phi) = -v\sin(2\phi) + 2(-\beta\cos(\phi) + \cos^2(\phi))\sigma. \quad (37)$$

Then, we subtract equation (36) from equation (37), which results in the following equation,

$$2\beta\dot{\phi}\cos(\phi) - 2(\delta^2 + \eta)\dot{\sigma} = 2\eta\dot{\psi} + (-2\beta\cos(\phi) + 4\alpha^2 + 2)\sigma. \quad (38)$$

Importantly, equation (38) has only two unknowns, $\phi(t)$ and $\sigma(t)$, and moreover it is linear in $\sigma(t)$. Now, replacing the second equation in the system (18) by (38), we obtain the following system,

$$\begin{aligned} \dot{\phi} &= \frac{1}{\beta}[-v\sin(\phi) + (-\beta + \cos(\phi))\sigma], \\ 2\beta\dot{\phi}\cos(\phi) - 2(\delta^2 + \eta)\dot{\sigma} &= 2\eta\dot{\psi} \\ &\quad + (-2\beta\cos(\phi) + 4\alpha^2 + 2)\sigma, \\ \dot{v} &= \delta\sigma^2 - 0.5\sigma\sin(2\phi) - 0.5(5 + \cos(2\phi))v. \end{aligned} \quad (39)$$

Next, we expand $\sin(\phi)$ and $\cos(\phi)$ in (39) as power series in ϕ , truncated to low orders, and obtain that

$$\dot{\phi} = \frac{1}{\beta}\left[-v\left(\phi - \frac{\phi^3}{6}\right) + \left(-\beta + 1 - \frac{\phi^2}{2}\right)\sigma\right] + O(\phi^4), \quad (40a)$$

$$\begin{aligned} 2\beta\dot{\phi}\left(1 - \frac{\phi^2}{2} + \frac{\phi^4}{24}\right) - 2(\delta^2 + \eta)\dot{\sigma} &= 2\eta\dot{\psi} + \left(-2\beta + \beta\phi^2 - \frac{\beta\phi^4}{12} + 4\alpha^2 + 2\right)\sigma \\ &\quad + O(\phi^6), \end{aligned} \quad (40b)$$

$$\dot{v} = \delta\sigma^2 - 0.5\sigma\left(2\phi - \frac{4}{3}\phi^3\right) - 3v + O(\phi^4). \quad (40c)$$

Note that unlike the expansion in orders of ε conducted above in Section 6, here we only expand the trigonometric expressions in ϕ . The orders of expansion for each expression in (40) were chosen as the minimal ones that enable obtaining the bifurcation condition.

Next, we use a method of harmonic balance [30], which allows us to obtain analytical expression for the pitchfork bifurcation. This method is based on the assumption that the

periodic solution for the steady-state of the system in (40) is a series of harmonic functions. Moreover, according to our numerical results (see Fig. 2(a)-(c)), $\phi(t)$ and $\sigma(t)$ are approximately single harmonic functions of ω , whereas v has the first two harmonic functions in ω . Thus, neglecting higher order harmonics, we may assume the following harmonic series solution:

$$\begin{aligned} \phi(t) &= \tilde{a}_0 + \tilde{a}_1\sin(\omega t) + \tilde{a}_2\cos(\omega t), \\ \sigma(t) &= \tilde{b}_0 + \tilde{b}_1\sin(\omega t) + \tilde{b}_2\cos(\omega t), \\ v(t) &= \tilde{c}_0 + \tilde{c}_1\sin(\omega t) + \tilde{c}_2\cos(\omega t) + \tilde{c}_3\sin(2\omega t) \\ &\quad + \tilde{c}_4\cos(2\omega t). \end{aligned} \quad (41)$$

By substituting the expansions given in equation (41) into (40) and equating the harmonics prefactors, one obtains a system of 11 algebraic equations with 11 unknowns, \tilde{a}_i , \tilde{b}_i , with $i = 0, 1, 2$, and \tilde{c}_i with $i = 0, 1, 2, 3, 4$.

Substituting (41) into equation (40b) and equating the coefficients of the first order harmonics, we get that the vector $\mathbf{b} = (\tilde{b}_0, \tilde{b}_1, \tilde{b}_2)^T$ may be expressed as a function of the vector $\mathbf{a} = (\tilde{a}_0, \tilde{a}_1, \tilde{a}_2)^T$ as follows,

$$\mathbf{M}_b(\mathbf{a})\mathbf{b} = \mathbf{F}_b(\mathbf{a}), \quad (42)$$

where $\mathbf{M}_b(\mathbf{a})$ and $\mathbf{F}_b(\mathbf{a})$ depend on the physical parameters of the problem and \mathbf{a} , see equations (B.1) and (B.3) in Appendix B. Thus, we may conclude that there exists a rational function \mathbf{B} , so that

$$\mathbf{b} = \mathbf{B}(\mathbf{a}), \quad (43)$$

where $\mathbf{B}(\mathbf{a}) = \mathbf{M}_b^{-1}(\mathbf{a})\mathbf{F}_b(\mathbf{a})$.

Now, since the equation in (40c) is linear in $v(t)$, substituting (41) into it, equating the coefficients of the first and second order harmonics, and using (43), we get that

$$\mathbf{M}_c\mathbf{c} = \mathbf{F}_c(\mathbf{a}, \mathbf{b}), \quad (44)$$

where $\mathbf{c} = (\tilde{c}_0, \tilde{c}_1, \tilde{c}_2, \tilde{c}_3, \tilde{c}_4)^T$. Note that \mathbf{M}_c depends only on ω , whereas \mathbf{F}_c depends on \mathbf{a} , \mathbf{b} , ω and the physical parameters of the problem. For more details, see equations (B.4) and (B.5) in Appendix B. Thus, we may conclude that there exists a rational function \mathbf{C} , so that

$$\mathbf{c} = \mathbf{C}(\mathbf{a}), \quad (45)$$

where $\mathbf{C}(\mathbf{a}) = \mathbf{M}_c^{-1}\mathbf{F}_c(\mathbf{a}, \mathbf{b} = \mathbf{B}(\mathbf{a}))$. Note that the linear dependence of \mathbf{b} on \mathbf{a} in (42) and of \mathbf{c} on \mathbf{a} in (44) is a simplification enabled only due to negligence of the term $2\delta v\sigma$ from the second equation in system (18).

In the last step, we substitute (41) into equation (40a), equate the coefficients of the first order harmonics, and use (43) and (45). Thus, we obtain a non-linear algebraic system of 3 equations,

$$\mathbf{F}(\mathbf{a}) = 0. \quad (46)$$

where \mathbf{F} is 3×1 vector, denoted by $(F_1(\mathbf{a}), F_2(\mathbf{a}), F_3(\mathbf{a}))^T$. F_1 is obtained from comparing coefficients for the free (DC) term in the harmonic balance equation (40a). It is proven in equations (B.6)–(B.10) in Appendix B that the equation $F_1(\mathbf{a}) = 0$ takes the form,

$$\tilde{a}_0 Y(\tilde{a}_0^2, \tilde{a}_1, \tilde{a}_2) = 0. \quad (47)$$

Equation (47) typically has two possible types of solutions for the unknowns \tilde{a}_0 , \tilde{a}_1 , and \tilde{a}_2 . The first type of solutions is with $\tilde{a}_0 = 0$, which corresponds to symmetric periodic solution of $\phi(t)$ according to (41). The second type of solutions is with $Y(\tilde{a}_0^2, \tilde{a}_1, \tilde{a}_2) = 0$ and $\tilde{a}_0^2 \neq 0$, which corresponds to a pair of asymmetric periodic solutions. The pitchfork bifurcation point occurs when the two types of solutions coincide, which means

$$\tilde{a}_0 = 0 \quad \text{and} \quad Y(0, \tilde{a}_1, \tilde{a}_2) = 0. \quad (48)$$

This can be interpreted as a bifurcation condition on ω and system parameters.

The bifurcation condition in (48), determines the parameter values where the symmetric periodic solution loses its stability. Hence, the bifurcation condition in (48) can be used in order to determine stability transition curve. In what follows, we present two methods that can be used to find the stability transition curve of the symmetric periodic solutions in the $(\delta\omega)$ -plane, in addition to the numerical calculation shown in Fig. 7, where the remaining parameters are fixed and given in Table 1.

In the first way, which we refer as to “numerical HB solution,” we find numerically the coefficients \tilde{a}_1 and \tilde{a}_2 , which satisfy the bifurcation condition in (48). More specifically, for any fixed δ , we use ‘fsolve’ function in Matlab and solve the following system of equations in the unknowns \tilde{a}_1 , \tilde{a}_2 , and ω :

$$\begin{cases} Y(0, \tilde{a}_1, \tilde{a}_2, \omega) = 0, \\ F_2(0, \tilde{a}_1, \tilde{a}_2, \omega) = 0, \\ F_3(0, \tilde{a}_1, \tilde{a}_2, \omega) = 0. \end{cases} \quad (49)$$

In particular, the solution of this system determines ω as a function of δ (and other parameters of the problem), for which the stability transition occurs.

In the second way, which we entitle “asymptotic,” we find an analytic approximation for the stability transition curve of the symmetric periodic solution, by using the perturbation expansion solution from equation (27). More specifically, we substitute a_1 and a_2 , given in (28), into the equation $Y(0, \tilde{a}_1, \tilde{a}_2, \omega) = 0$ namely, we substitute $\tilde{a}_i = \varepsilon a_i$ for $i = 1, 2$, where $\varepsilon = A\eta\omega^2$ and a_i are given in (28). This gives a high-degree polynomial in ω , where the rest of parameters are fixed. This equation is an approximation of the bifurcation condition in (48). In order to reduce the complexity of this equation, we further approximate a_1 and a_2 , by defining

another small parameter $\tilde{\varepsilon} = \sqrt{(\delta^2 + \eta)} \ll 1$ and assuming that $\eta \ll \delta$ so that $\eta = O(\tilde{\varepsilon}^2)$, and $\alpha = O(\sqrt{\tilde{\varepsilon}})$. Hence, if we define

$$\tilde{\alpha} = \frac{\alpha}{\sqrt{\tilde{\varepsilon}}}, \quad \tilde{\eta} = \frac{\eta}{\tilde{\varepsilon}^2}, \quad (50)$$

we may expand a_1 and a_2 given in (28), in $\tilde{\varepsilon}$ as follows

$$\begin{aligned} a_1 &= \frac{(-1 + \beta)}{4\tilde{\alpha}^4\beta} - \frac{(\omega^2(-1 + \beta))\tilde{\varepsilon}^2}{16(\tilde{\alpha}^8\beta)} + O(\tilde{\varepsilon}^4), \\ a_2 &= \frac{\beta - 1}{2\omega\tilde{\alpha}^2\beta\tilde{\varepsilon}} - \frac{\omega\tilde{\varepsilon}(\beta - 1)}{8\tilde{\alpha}^6\beta} + \frac{\omega^3(-1 + \beta)\tilde{\varepsilon}^3}{32\tilde{\alpha}^{10}\beta} + O(\tilde{\varepsilon}^4). \end{aligned} \quad (51)$$

Substituting the assumptions in (50) and (51) into the numerator of (the rational) equation $Y(0, \tilde{a}_1, \tilde{a}_2, \omega) = 0$, and expanding the numerator of the resulting function in $\tilde{\varepsilon}$ and ε up to orders $O(\tilde{\varepsilon}^3)$ and $O(\varepsilon^3)$, respectively, we obtain that the stability transition curve may be approximated by a polynomial in two variables δ and ω ,

$$d_8(\delta)\omega^8 + d_6(\delta)\omega^6 + d_4(\delta)\omega^4 + d_2(\delta)\omega^2 + d_0(\delta) = 0, \quad (52)$$

where the rest of parameters are given in Table 1, and d_8 , d_6 , d_4 , d_2 , and d_0 are polynomials in δ . The complete calculation can be found in symbolic Matlab code, which is provided in the supplementary information (SI) [19]. In Appendix B (see (B.11)), we give the numerical values of the coefficients for the physical parameters which are as given in Table 1, nondimensional scaling in (17), and amplitude $A = 0.1$. To obtain the bifurcation point $\omega(\delta)$, where the symmetric periodic solution loses its stability, we need to find the corresponding root of the bi-quartic polynomial in (52). For each δ , there are up to four roots for ω^2 , where negative and complex-valued roots are discarded. The rest of roots (except one root, which we denote by $\omega(\delta)$) are far from the numerical solution of the harmonic balance equations. Thus, the red curve in Fig. 10 was obtained by plotting the roots $\omega(\delta)$, which are the closest to the numerical solution of the harmonic balance equations.

In Fig. 10 we show the stability transition curve obtained by using the abovementioned three ways: the numerical one as shown in Fig. 7, Numerical HB, and Asymptotic. It can be seen that there is an excellent agreement between all of them, where for sufficiently small values of δ the numerical and Numerical HB solutions nearly coincide. The dependence of the stability transition curves (see, numerical and Numerical HB solutions) on the amplitude A is relatively small, and it decreases as δ increases. Even though the asymptotic solution misses the dependence of the stability curve on the amplitude A (both values of A , $A = 0.1$ and $A = 0.5$ [rad] yield the same curve), it still captures well the

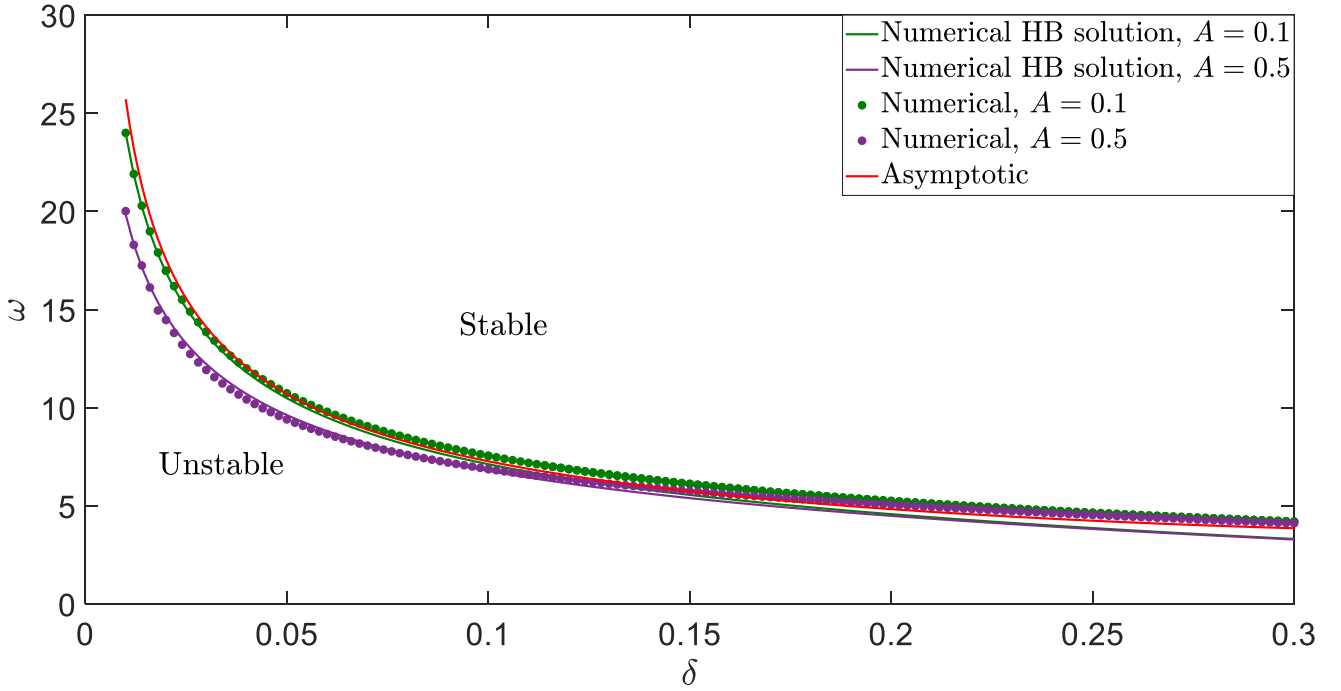


Fig. 10: Stability transition curve obtained on (δ, ω) -plane. Numerical HB solution for the amplitude of $A \in \{0.1, 0.5\}$ [rad] which satisfies the criterion defined in (48), is denoted by green and purple solid curves, respectively. Numerical calculation of the stability transition curve by finding symmetric periodic solution (i.e finding fixed point of the Poincaré map) and calculating its Floquet multipliers (as in equation (20) and graph in Fig. 7) for the amplitude of $A \in \{0.1, 0.5\}$ [rad] is denoted by green and purple circles. Asymptotic solution denoted by red solid curve, was obtained by finding the roots of the closed-form polynomial given in (52), and is approximately independent of A in the range $A \in [0.1, 0.5]$. Above the stability transition curve, the symmetric periodic solution is stable, and below it is unstable.

monotonic decrease of ω as a function of δ along the stability curve. The asymptotic curve is very close to both other methods, where for sufficiently large δ it approximates the numerical solution even better than Numerical HB method. The main advantage of the asymptotic solution is its simplicity, which allows to obtain a very good approximation for the stability curve via finding roots of a closed-form polynomial.

8 Concluding remarks

In this study we investigated the dynamics of a rotor-actuated Twistcar robot with passive steering joint. We formulated the system's nonlinear dynamic equations of motion and performed numerical simulations. Our results revealed that there exists an optimal rotor's COM position which maximizes the mean speed of the robot. Moreover, upon varying the actuation frequency ω or rotor's COM position, we showed that there exist two bifurcation points of periodic solutions, one of the type “pitchfork” and the second of the type “fold.” For the frequency smaller than the “pitchfork” critical frequency, there exists a pair of stable asymmetric

periodic solutions and an unstable primary symmetric periodic solution. When ω is increased beyond the “pitchfork” bifurcation point, the primary symmetric periodic solution becomes stable and a pair of unstable asymmetric periodic solutions emerge. Increasing the frequency even more, we achieve a “fold” bifurcation, where the stable and unstable asymmetric periodic solutions meet. For frequency larger than the “fold” bifurcation value, there exists only a stable symmetric periodic solution. For a constant frequency, but varying rotor's COM location, we obtain a similar picture of periodic solutions' multiplicity and bifurcations as described above. Thus, by using Poincaré map we constructed a stability transition map of the primary symmetric periodic solution in the frequency and rotor's COM position plane.

In addition, we used asymptotic tools which allowed us to obtain approximate explicit expressions describing the behavior of the system. In particular, the perturbation analysis yielded an approximate solution for the symmetric branch, which allowed to find an analytical expression for the optimal rotor's COM location. By using harmonic balance, we obtained an approximation for the bifurcation points of pitchfork type. Finally, based on the combination between

perturbation analysis and harmonic balance we formulated an analytic approximation for the stability transitions criterion as a function of frequency and rotor's COM location. We compared between the analytical and numerical results and obtained a very good agreement.

The results illustrate the rich dynamics observed in periodically-actuated systems with a passive shape coordinate. In addition, our work proves the significant contribution of asymptotic analysis for finding explicit formulation of some of the system's dynamic phenomena. Future work will attempt to demonstrate some of the theoretical results in experiments using wheeled articulated robotic vehicles.

Supplementary information

Supplementary material related to this article can be found online at <https://yizhar.net.technion.ac.il/files/2025/06/SI-MATLAB-file-Anna-Z.zip>. The Matlab code for reproducing the results in Fig. 10 and in particular the calculation of the coefficients which appear in equation (52) is available electronically in the supplementary information (SI).

Acknowledgments

We wish to warmly thank Prof. Oleg Gendelman for many fruitful discussions and insights. The work of Y. O. has been supported by Israel Science Foundation under grant no. 1382/23.

Data availability The datasets generated during and/or analysed during the current study are available from the corresponding author on reasonable request.

Declarations

Conflict of interests The authors declare that they have no conflicts of interest.

Appendix A

Under the assumption of $m_1 = m_2 = I_1 = I_2 = 0$, the matrices in (14) can be expressed explicitly as,

$$\mathbf{M}_r = \begin{bmatrix} m_r & 0 & 0 \\ 0 & J_r + b_1^2 m_r & J_r \\ 0 & J_r & J_r \end{bmatrix}, \quad (\text{A.1})$$

$$\mathbf{B}_r = \begin{bmatrix} -b_1 m_r \dot{\theta}^2 \\ b_1 m_r v \dot{\theta} \\ 0 \end{bmatrix}, \quad (\text{A.2})$$

and

$$\mathbf{D}_r = c \begin{bmatrix} (2 + \cos^2 \phi) v + \frac{l_1}{2} \sin(2\phi) \dot{\theta} \\ \frac{l_1}{2} v + (2s^2 + l_1^2 \sin^2 \phi) \dot{\theta} \\ 0 \end{bmatrix}. \quad (\text{A.3})$$

Appendix B

Here we give all details of the derivations in Section 7. Let us start from the matrix $\mathbf{M}_b(\mathbf{a})$ appearing in equation (42). Substituting the expansions given in (41) into equation (40b), it is possible to verify that is given by,

$$\mathbf{M}_b = \begin{bmatrix} m_{1,1} & m_{1,2} & m_{1,3} \\ -m_{1,2} & m_{2,2} & m_{2,3} \\ -m_{1,3} & m_{3,2} & m_{3,3} \end{bmatrix}, \quad (\text{B.1})$$

where

$$\begin{aligned} m_{1,1} &= \beta \left(\tilde{a}_0^2 + \frac{\tilde{a}_1^2}{2} + \frac{\tilde{a}_2^2}{2} \right) - 2\beta - \frac{\beta}{96} (8\tilde{a}_0^4 + 24\tilde{a}_0^2 \tilde{a}_1^2 + 24\tilde{a}_0^2 \tilde{a}_2^2 + 3\tilde{a}_1^4 + 6\tilde{a}_1^2 \tilde{a}_2^2 + 3\tilde{a}_2^4) + 4\alpha^2 + 2, \\ m_{1,2} &= \tilde{a}_0 \tilde{a}_1 \beta - \frac{\tilde{a}_0 \tilde{a}_1 \beta}{24} (4\tilde{a}_0^2 + 3\tilde{a}_1^2 + 3\tilde{a}_2^2), \\ m_{1,3} &= \tilde{a}_0 \tilde{a}_2 \beta - \frac{\tilde{a}_0 \tilde{a}_2 \beta}{24} (4\tilde{a}_0^2 + 3\tilde{a}_1^2 + 3\tilde{a}_2^2), \\ m_{2,2} &= -2\alpha^2 + \beta + \frac{\beta}{192} (8\tilde{a}_0^4 + 36\tilde{a}_0^2 \tilde{a}_1^2 + 12\tilde{a}_0^2 \tilde{a}_2^2 + 5\tilde{a}_1^4 + 6\tilde{a}_1^2 \tilde{a}_2^2 + \tilde{a}_2^4) - \beta \left(\frac{\tilde{a}_0^2}{2} + \frac{3\tilde{a}_1^2}{8} + \frac{\tilde{a}_2^2}{8} \right) - 1, \\ m_{2,3} &= \omega(\delta^2 + \eta) - \frac{\tilde{a}_1 \tilde{a}_2 \beta}{4} + \frac{\tilde{a}_1 \tilde{a}_2 \beta}{48} (6\tilde{a}_0^2 + \tilde{a}_1^2 + \tilde{a}_2^2), \\ m_{3,2} &= \frac{\tilde{a}_1 \tilde{a}_2 \beta}{48} (6\tilde{a}_0^2 + \tilde{a}_1^2 + \tilde{a}_2^2) - \frac{\tilde{a}_1 \tilde{a}_2 \beta}{4} - \omega(\delta^2 + \eta), \\ m_{3,3} &= -2\alpha^2 + \beta + \frac{\beta}{192} (8\tilde{a}_0^4 + 12\tilde{a}_0^2 \tilde{a}_1^2 + 36\tilde{a}_0^2 \tilde{a}_2^2 + \tilde{a}_1^4 + 6\tilde{a}_1^2 \tilde{a}_2^2 + 5\tilde{a}_2^4) - \beta \left(\frac{\tilde{a}_0^2}{2} + \frac{\tilde{a}_1^2}{8} + \frac{3\tilde{a}_2^2}{8} \right) - 1. \end{aligned} \quad (\text{B.2})$$

Similarly, we get that the forcing term vector $\mathbf{F}_b(\mathbf{a})$ appearing in equation (42) is given by

$$\mathbf{F}_b(\mathbf{a}) = \frac{1}{192} \begin{bmatrix} 0 \\ 192(A\eta\omega^2 - \tilde{a}_2\beta\omega) - \tilde{a}_2\beta\omega(8\tilde{a}_0^4 + 12\tilde{a}_0^2 \tilde{a}_1^2 + 12\tilde{a}_0^2 \tilde{a}_2^2 + \tilde{a}_1^4 + 2\tilde{a}_1^2 \tilde{a}_2^2 + \tilde{a}_2^4) + 4\tilde{a}_2\beta\omega(4\tilde{a}_0^2 + \tilde{a}_1^2 + \tilde{a}_2^2) \\ 192\tilde{a}_1\beta\omega + \tilde{a}_1\beta\omega(8\tilde{a}_0^4 + 12\tilde{a}_0^2 \tilde{a}_1^2 + 12\tilde{a}_0^2 \tilde{a}_2^2 + \tilde{a}_1^4 + 2\tilde{a}_1^2 \tilde{a}_2^2 + \tilde{a}_2^4) - 24\tilde{a}_1\beta\omega(4\tilde{a}_0^2 + \tilde{a}_1^2 + \tilde{a}_2^2) \end{bmatrix}. \quad (\text{B.3})$$

Next, substituting the expansions given in (41) into equation (40c), it is possible to verify that the matrix $\mathbf{M}_c(\mathbf{a})$ appearing in equation (44) is given by

$$\mathbf{M}_c = \begin{bmatrix} 3 & 0 & 0 & 0 & 0 \\ 0 & -0.5\omega & -1.5 & 0 & 0 \\ 0 & -1.5 & 0.5\omega & 0 & 0 \\ 0 & 0 & 0 & -\omega & -1.5 \\ 0 & 0 & 0 & -1.5 & \omega \end{bmatrix}. \quad (\text{B.4})$$

In addition, the forcing term vector $\mathbf{F}_c(\mathbf{a}, \mathbf{b})$ appearing in equation (44) is given by

$$\mathbf{F}_c(\mathbf{a}, \mathbf{b}) = \frac{1}{12} \begin{bmatrix} 8\tilde{a}_0^3\tilde{b}_0 + 12\tilde{a}_0^2\tilde{a}_1\tilde{b}_1 + 12\tilde{a}_0^2\tilde{a}_2\tilde{b}_2 + 12\tilde{a}_012\tilde{a}_1^2\tilde{b}_0 + 12\tilde{a}_0\tilde{a}_2^2\tilde{b}_0 - 12\tilde{a}_0\tilde{b}_0 + 3\tilde{a}_1^3\tilde{b}_1 + 3\tilde{a}_1^2\tilde{a}_2\tilde{b}_2 + 3\tilde{a}_1\tilde{a}_2^2\tilde{b}_1 - 6\tilde{a}_1\tilde{b}_1 + 3\tilde{a}_2^3\tilde{b}_2 - 6\tilde{a}_2\tilde{b}_2 + 12\delta\tilde{b}_0^2 + 6\delta\tilde{b}_1^2 + 6\delta\tilde{b}_2^2 \\ 4\tilde{b}_2\tilde{a}_0^3 + 12\tilde{b}_0\tilde{a}_0^2\tilde{a}_2 + 3\tilde{b}_2\tilde{a}_0\tilde{a}_1^2 + 6\tilde{b}_1\tilde{a}_0\tilde{a}_1\tilde{a}_2 + 9\tilde{b}_2\tilde{a}_0\tilde{a}_2^2 - 6\tilde{b}_2\tilde{a}_0 + 3\tilde{b}_0\tilde{a}_1^2\tilde{a}_2 + 3\tilde{b}_0\tilde{a}_2^3 - 6\tilde{b}_0\tilde{a}_2 + 12\tilde{b}_0\tilde{b}_2\delta \\ 4\tilde{b}_1\tilde{a}_0^3 + 12\tilde{b}_0\tilde{a}_0^2\tilde{a}_1 + 9\tilde{b}_1\tilde{a}_0\tilde{a}_1^2 + 6\tilde{b}_2\tilde{a}_0\tilde{a}_1\tilde{a}_2 + 3\tilde{b}_1\tilde{a}_0\tilde{a}_2^2 - 6\tilde{b}_1\tilde{a}_0 + 3\tilde{b}_0\tilde{a}_1^3 + 3\tilde{b}_0\tilde{a}_1\tilde{a}_2^2 - 6\tilde{b}_0\tilde{a}_1 + 12\tilde{b}_0\tilde{b}_1\delta \\ 6\tilde{b}_2\tilde{a}_0^2\tilde{a}_2 - 6\tilde{a}_1\tilde{b}_1\tilde{a}_0^2 + 6\tilde{b}_0\tilde{a}_0\tilde{a}_2^2 - 6\tilde{a}_1^2\tilde{b}_0\tilde{a}_0 + 2\tilde{b}_2\tilde{a}_2^3 - 3\tilde{b}_2\tilde{a}_2 + 3\tilde{a}_1\tilde{b}_1 - 3\delta(\tilde{b}_1^2 - \tilde{b}_2^2) - 2\tilde{a}_1^3\tilde{b}_1 \\ 6\tilde{b}_2\tilde{a}_0^2\tilde{a}_1 + 6\tilde{b}_1\tilde{a}_0^2\tilde{a}_2 + 12\tilde{b}_0\tilde{a}_0\tilde{a}_1\tilde{a}_2 + \tilde{b}_2\tilde{a}_1^3 + 3\tilde{b}_1\tilde{a}_1^2\tilde{a}_2 + 3\tilde{b}_2\tilde{a}_1\tilde{a}_2^2 - 3\tilde{b}_2\tilde{a}_1 + \tilde{b}_1\tilde{a}_2^3 - 3\tilde{b}_1\tilde{a}_2 + 6\tilde{b}_1\tilde{b}_2\delta \end{bmatrix}. \quad (\text{B.5})$$

In order to justify the expression for \tilde{a}_0 which was given in (47), let us consider the equation for \tilde{a}_0 in the system (46), which follows from the harmonic balance of the equation in (40a). It is possible to verify that this equation is given by,

$$F_1(\tilde{a}_0, \tilde{a}_1, \tilde{a}_2) = \frac{\tilde{a}_0^3\tilde{c}_0}{6} - \frac{\tilde{a}_1\tilde{c}_1}{2} - \frac{\tilde{a}_2\tilde{c}_2}{2} - \frac{\tilde{a}_0^2\tilde{b}_0}{2} - \frac{\tilde{a}_1^2\tilde{b}_0}{4} - \frac{\tilde{a}_2^2\tilde{b}_0}{4} - \tilde{a}_0\tilde{c}_0 + \frac{\tilde{a}_1^3\tilde{c}_1}{16} + \frac{\tilde{a}_2^3\tilde{c}_2}{16} - \tilde{b}_0(\beta - 1) - \frac{\tilde{a}_0\tilde{a}_1\tilde{b}_1}{2} \\ - \frac{\tilde{a}_0\tilde{a}_2\tilde{b}_2}{2} + \frac{\tilde{a}_0\tilde{a}_1^2\tilde{c}_0}{4} + \frac{\tilde{a}_0\tilde{a}_2^2\tilde{c}_0}{4} + \frac{\tilde{a}_0^2\tilde{a}_1\tilde{c}_1}{4} + \frac{\tilde{a}_1\tilde{a}_2^2\tilde{c}_1}{16} + \frac{\tilde{a}_0^2\tilde{a}_2\tilde{c}_2}{4} - \frac{\tilde{a}_0\tilde{a}_1^2\tilde{c}_4}{8} + \frac{\tilde{a}_1^2\tilde{a}_2\tilde{c}_2}{16} + \frac{\tilde{a}_0\tilde{a}_2^2\tilde{c}_4}{8} + \frac{\tilde{a}_0\tilde{a}_1\tilde{a}_2\tilde{c}_3}{4} = 0. \quad (\text{B.6})$$

Now, using the definition of \mathbf{b} and the expressions in (B.1)–(B.3), it is possible to verify that \tilde{b}_0 , \tilde{b}_1 , and \tilde{b}_2 take the form

$$\begin{aligned} \tilde{b}_0 &= \tilde{a}_0 g_0(\tilde{a}_0^2, \tilde{a}_1, \tilde{a}_2), \\ \tilde{b}_i &= g_i(\tilde{a}_0^2, \tilde{a}_1, \tilde{a}_2), \quad i = 1, 2, \end{aligned} \quad (\text{B.7})$$

where $g_i(\tilde{a}_0^2, \tilde{a}_1, \tilde{a}_2)$, $i = 0, 1, 2$, are rational functions of \tilde{a}_0^2 , which are not singular at $\tilde{a}_0 = 0$. In order to prove that (B.7) holds, let us consider the inverse matrix $\mathbf{M}_b^{-1}(\mathbf{a}) = (\xi_{i,j})_{1 \leq i,j \leq 3}$ and the forcing term vector $\mathbf{F}_b(\mathbf{a}) = (0, \varphi_2(\mathbf{a}), \varphi_3(\mathbf{a}))^T$, where $\mathbf{M}_b(\mathbf{a})$ and $\mathbf{F}_b(\mathbf{a})$ are given explicitly in (B.1)–(B.3). Note that b_i , $i = 0, 1, 2$, are obtained as follows

$$b_i = (\xi_{i+1,2}, \xi_{i+1,3}) \cdot (\varphi_2(\mathbf{a}), \varphi_3(\mathbf{a})). \quad (\text{B.8})$$

Now, it is easy to verify that the elements of the matrix $\mathbf{M}_b^{-1}(\mathbf{a})$ are rational functions of the form,

$$\begin{aligned} \xi_{1,j} &= \tilde{a}_0 \xi_{1,j}(\tilde{a}_0^2, \tilde{a}_1, \tilde{a}_2), \quad j = 2, 3, \\ \xi_{i,j} &= \xi_{i,j}(\tilde{a}_0^2, \tilde{a}_1, \tilde{a}_2), \quad i, j = 2, 3, \end{aligned} \quad (\text{B.9})$$

which are not singular at $\tilde{a}_0 = 0$. Moreover, note that $\varphi_2(\mathbf{a})$ and $\varphi_3(\mathbf{a})$ are polynomials in \tilde{a}_0^2 . Hence, from (B.3), (B.8), and (B.9), we may conclude that (B.7) holds.

Next, note that the matrix \mathbf{M}_c , which is given in (B.4), is independent of \tilde{a}_0 . Hence, looking on (B.5) and using (B.7), we may conclude that there exists rational functions w_i , $i = 0, 1, 2, 3, 4$, of \tilde{a}_0^2 , which are not singular at $\tilde{a}_0 = 0$, so that

$$\begin{aligned} \tilde{c}_i &= w_i(\tilde{a}_0^2, \tilde{a}_1, \tilde{a}_2), \quad i = 0, 3, 4, \\ \tilde{c}_i &= \tilde{a}_0 w_i(\tilde{a}_0^2, \tilde{a}_1, \tilde{a}_2), \quad i = 1, 2. \end{aligned} \quad (\text{B.10})$$

Finally, substituting (B.7) and (B.10) into (B.6), we may conclude that \tilde{a}_0 is of the form that was given in (47).

For $A = 0.1$, $\alpha = \beta = 1/3$, $\eta = 0.0118$, we get that the stability transition curve may be approximated by the following polynomial, which are rounded to fifth digit

$$\begin{aligned} d_8(\delta) &\approx -9.0195 \cdot 10^{-3} \delta^7 + 4.7409 \cdot 10^{-4} \delta^5 + 1.4956 \cdot 10^{-5} \delta^3 + 9.5651 \cdot 10^{-7} \delta, \\ d_6(\delta) &\approx -1439.5 \delta^8 - 3.5514 \cdot 10^{-2} \delta^7 - 67.943 \delta^6 + 189.61 \delta^5 - 1.2026 \delta^4 + 4.48 \delta^3 \\ &\quad - 9.4604 \cdot 10^{-3} \delta^2 + 2.6596 \cdot 10^{-2} \delta - 2.7908 \cdot 10^{-5}, \\ d_4(\delta) &\approx -3238.8 \delta^8 - 152.87 \delta^6 + 2132.7 \delta^5 - 2277.4 \delta^4 + 50.353 \delta^3 - 53.705 \delta^2 + 150.08 \delta - 0.3168, \\ d_2(\delta) &\approx 3838.61 \delta^5 - 5118.1 \delta^4 + 90.591 \delta^3 - 120.79 \delta^2 + 1685.52 \delta - 899.37, \\ d_0(\delta) &\approx 3032.907 \delta - 2021.98. \end{aligned} \quad (\text{B.11})$$

References

1. E. M. Artemova and I. A. Bizyaev. Dynamics of a multilink wheeled vehicle: partial solutions and unbounded speedup. *International Journal of Non-Linear Mechanics*, 165:104774, 2024.
2. S. Bazzi, E. Shammass, D. Asmar, and M. T. Mason. Motion analysis of two-link nonholonomic swimmers. *Nonlinear Dynamics*, 89(4):2739—2751, 2017.
3. L. E. Becker, S. A. Koehler, and H. A. Stone. On self-propulsion of micro-machines at low Reynolds number: Purcell’s three-link swimmer. *Journal of Fluid Mechanics*, 490:15–35, 2003.
4. I. A. Bizyaev, A. V. Borisov, and S. P. Kuznetsov. The Chaplygin sleigh with friction moving due to periodic oscillations of an internal mass. *Nonlinear Dynamics*, 95(1):699—714, 2019.
5. I. A. Bizyaev, A. V. Borisov, and I. S. Mamaev. Exotic dynamics of nonholonomic roller racer with periodic control. *Regular and Chaotic Dynamics*, 23(7):983—994, 2018.
6. A. M. Bloch. *Basic Concepts in Geometric Mechanics*. Springer New York, New York, NY, 2003.
7. O. Chakon and Y. Or. Analysis of underactuated dynamic locomotion systems using perturbation expansion: The twistcar toy example. *Journal of Nonlinear Science*, 27(4):1215—1234, 2017.
8. S. A. Chaplygin. The theory of the motion of non-holonomic systems: Examples of the use of the reducing factor method. In *Collected Papers*, volume 3, pages 248–259. Gostekhizdat, Moscow–Leningrad, 1950.
9. S. Chitta, P. Cheng, E. Frazzoli, and V. Kumar. Robotrikke: A novel undulatory locomotion system. In *Proceedings of the 2005 IEEE International Conference on Robotics and Automation*, pages 1597–1602. IEEE, 2005.
10. T. Dear, B. Buchanan, R. Abraján-Guerrero, S. D. Kelly, M. Travers, and H. Choset. Locomotion of a multi-link non-holonomic snake robot with passive joints. *The International Journal of Robotics Research*, 39(5):598–616, 2020.
11. T. Dear, S. D. Kelly, M. Travers, and H. Choset. Locomotive analysis of a single-input three-link snake robot. In *2016 IEEE 55th Conference on Decision and Control (CDC)*, pages 7542–7547, 2016.
12. V. Fedonyuk and P. Tallapragada. Stick-slip motion of the Chaplygin sleigh with a piecewise-smooth nonholonomic constraint. *Journal of Computational and Nonlinear Dynamics*, 12(3):031021, 2017.
13. V. Fedonyuk and P. Tallapragada. Sinusoidal control and limit cycle analysis of the dissipative Chaplygin sleigh. *Nonlinear Dynamics*, 93:835–846, 2018.
14. J. Guckenheimer and P. Holmes. *Nonlinear Oscillations, Dynamical Systems, and Bifurcations of Vector Fields*, volume 42. Springer, 1983.
15. E. Gutman and Y. Or. Symmetries and gaits for Purcell’s three-link microswimmer model. *IEEE Transactions on Robotics*, 32(1):53–69, 2016.
16. O. Halvani and Y. Or. Nonholonomic dynamics of the Twistcar vehicle: asymptotic analysis and hybrid dynamics of frictional skidding. *Journal of Nonlinear Science*, 107(4):3443–3459, 2022.
17. Y. Harduf, D. Jin, Y. Or, and L. Zhang. Nonlinear parametric excitation effect induces stability transitions in swimming direction of flexible superparamagnetic microswimmers. *Soft Robotics*, 5(4):389–398, 2018.
18. R. L. Hatton and H. Choset. Geometric swimming at low and high Reynolds numbers. *IEEE Transactions on Robotics*, 29(3):615–624, 2013.
19. See Supporting Information. Supporting information for “Dynamics and multi-stability of a rotor-actuated twistcar robot with passive steering joint” is available at <https://yizhar.net.technion.ac.il/files/2025/06/SI-MATLAB-file-Anna-Z.zip>. 2025.
20. E. Kanso, J. E. Marsden, C. W. Rowley, and J. B. Melli-Huber. Locomotion of articulated bodies in a perfect fluid. *Journal of Nonlinear Science*, 15(4):255–289, 2005.
21. S. D. Kelly, M. J. Fairchild, P. M. Hasing, and P. Tallapragada. Proportional heading control for planar navigation: The Chaplygin beanie and fishlike robotic swimming. In *2012 American Control Conference (ACC)*, pages 4885–4890, 2012.
22. S. D. Kelly and R. M. Murray. Geometric phases and robotic locomotion. *Journal of Robotic Systems*, 12(6):417–431, 1995.
23. A. A. Kilin, T. B. Ivanova, Y. L. Karavaev, and K. S. Yefremov. Theoretical and experimental investigations of the controlled motion of a roller racer. *Theoretical and Applied Mechanics*, 2025.
24. P. S. Krishnaprasad and D. P. Tsakiris. Oscillations, SE(2)-snakes and motion control. In *Proceedings of 1995 34th IEEE Conference on Decision and Control*, volume 3, pages 2806–2811 vol.3, 1995.
25. R. Levy, A. Dantus, Z. Yu, and Y. Or. Analysis and experiments of the dissipative Twistcar-direction reversal and asymptotic approximations. *arXiv preprint arXiv:2506.19112*, 2025.
26. D. G. Macharet, A. A. Neto, V. F. da Camara Neto, and M. F. M. Campos. Nonholonomic path planning optimization for Dubins’ vehicles. In *2011 IEEE International Conference on Robotics and Automation*, pages 4208–4213, 2011.
27. R. M. Murray, Z. Li, and S. S. Sastry. *A Mathematical Introduction to Robotic Manipulation*. CRC Press, 1994.
28. Y. Nakamura, H. Ezaki, Y. Tan, and W. Chung. Design of steering mechanism and control of nonholonomic trailer systems. *IEEE transactions on Robotics and Automation*, 17(3):367–374, 2001.
29. A. H. Nayfeh. *Perturbation Methods*. John Wiley & Sons, 2008.
30. A. H. Nayfeh and D. T. Mook. *Nonlinear Oscillations*. John Wiley & Sons, 2008.
31. J. Neimark and N. Fufaev. *Dynamics of Nonholonomic Systems (Translations of Mathematical Monographs)*, volume 33. Amer. Mathematical Society, 1972.
32. J. M. Osborne and D. V. Zenkov. Steering the Chaplygin sleigh by a moving mass. In *Proceedings of the 44th IEEE Conference on Decision and Control*, pages 1114–1118, 2005.
33. J. Ostrowski and J. Burdick. The geometric mechanics of undulatory robotic locomotion. *The international Journal of Robotics Research*, 17(7):683–701, 1998.
34. J. Ostrowski, J. Burdick, A.D. Lewis, and R.M. Murray. The mechanics of undulatory locomotion: the mixed kinematic and dynamic case. In *Proceedings of 1995 IEEE International Conference on Robotics and Automation*, volume 2, pages 1945–1951 vol.2, 1995.
35. J. Ostrowski, A. Lewis, R. Murray, and J. Burdick. Nonholonomic mechanics and locomotion: the snakeboard example. In *Proceedings of the 1994 IEEE International Conference on Robotics and Automation*, pages 2391–2397 vol.3, 1994.
36. T. Pardi, V. Maddali, V. Ortenzi, R. Stolkin, and N. Marturi. Path planning for mobile manipulator robots under non-holonomic and task constraints. In *2020 IEEE/RSJ International Conference on Intelligent Robots and Systems (IROS)*, pages 6749–6756. IEEE, 2020.
37. J. Paul, Y. Or, and O. V. Gendelman. Nonlinear dynamics and bifurcations of a planar undulating magnetic microswimmer. *Physical Review E*, 107:054211, 2023.
38. L. Rizyaev and Y. Or. Locomotion dynamics of an underactuated three-link robotic vehicle. *arXiv preprint arXiv:2407.21540*, 2024.
39. C. Rodwell and P. Tallapragada. Induced and tunable multistability due to nonholonomic constraints. *Nonlinear Dynamics*, 108:2115—2126, 2022.
40. H. Salman, T. Dear, S. Babikian, E. Shammass, and H. Choset. A physical parameter-based skidding model for the snakeboard. In *2016 IEEE 55th Conference on Decision and Control (CDC)*, pages 7555–7560. IEEE, 2016.

41. E. A. Shammass, H. Choset, and A. A. Rizzi. Geometric motion planning analysis for two classes of underactuated mechanical systems. *The International Journal of Robotics Research*, 26(10):1043–1073, 2007.
42. S. V. Stanchenko. Non-holonomic Chaplygin systems. *Journal of Applied Mathematics and Mechanics*, 53(1):11–17, 1989.
43. P. Tallapragada and V. Fedonyuk. Steering a Chaplygin sleigh using periodic impulses. *Journal of Computational and Nonlinear Dynamics*, 12(5):054501, 2017.
44. E. Tovi, A. Zigelman, and Y. Or. Dynamics, stability and bifurcations of a planar three-link swimmer with passive visco-elastic joint using “ideal fluid” model. *International Journal of Non-Linear Mechanics*, 167:104859, 2024.
45. H. Yang, S. X. Yang, and G. S. Mittal. Tracking control of a nonholonomic mobile robot by integrating feedback and neural dynamics techniques. In *Proceedings 2003 IEEE/RSJ International Conference on Intelligent Robots and Systems (IROS 2003)*(Cat. No. 03CH37453), volume 4, pages 3522–3527. IEEE, 2003.
46. T. Yona and Y. Or. The wheeled three-link snake model: singularities in nonholonomic constraints and stick-slip hybrid dynamics induced by Coulomb friction. *Nonlinear Dynamics*, 95(3):2307–2324, 2019.
47. A. Zigelman, G. Ben Zvi, and Y. Or. Dynamics of Purcell-type microswimmers with active-elastic joints. *Phys. Rev. E*, 110:014207, 2024.